The Astronomical Journal, 169:334 (22pp), 2025 June https://doi.org/10.3847/1538-3881/adccc6

# A Swarm of WASP Planets: Nine Giant Planets Identified by the WASP Survey

N. Schanche[1,2], G. Hébrard[3,4], K. G. Stassun[5], B. Hord[2,44], K. Barkaoui[6,7,8], A. Bieryla[9], D. Ciardi[10], K. A. Collins[9], A. Collier Cameron[11], J. Hartman[12], N. Heidari[3], C. Hellier[13], S. B. Howell[14], M. Lendl[15], J. McCormac[16,17], K. K. McLeod[18], H. Parviainen[8,19], D. Radford[20], A. S. Rajpurohit[21], H. Relles[9], R. Sharma[21], S. Baliwal[21,22], G. Bakos[12], S. C. C. Barros[23], F. Bouchy[15], A. Burdanov[7], P. A. Budnikova[24], A. Chakaraborty[21], C. Clark[10,25], Laetitia Delrez[6,26,27], O. D. S. Demangeon[23], R. F. Díaz[28], J. Donnenfield[12,29], M. Everett[30], A. Fukui[31,32], M. Gillon[6], C. Hedges[2,33], J. Higuera[30], E. Jehin[26], J. M. Jenkins[14], F. Kiefer[34], D. Laloum[35], J. Livingston[36,37,38], M. Lund[10], P. Magain[39], P. Maxted[13], I. Mireles[40], F. Murgas[32,41], N. Narita[31,32,36], K. J. Nikitha[21], C. Opitom[42], E. Palle[32,41], Y. G. Patel[30], M. Rose[14], S. G. Sousa[23], I. A. Strakhov[24], P. Strøm[16], A. Tuson[2,33], R. West[43], and J. Winn[12]

[1] Department of Astronomy, University of Maryland, College Park, MD 20742, USA; nicole.e.schanche@nasa.gov
[2] NASA Goddard Space Flight Center, 8800 Greenbelt Road, Greenbelt, MD 20771, USA
[3] Institut d'astrophysique de Paris, UMR7095 CNRS, Université Pierre & Marie Curie, 98bis boulevard Arago, 75014 Paris, France
[4] Observatoire de Haute-Provence, CNRS, Université d'Aix-Marseille, 04870 Saint-Michel-l'Observatoire, France
[5] Department of Physics & Astronomy, Vanderbilt University, 6301 Stevenson Center Lane, Nashville, TN 37235, USA
[6] Astrobiology Research Unit, Université de Liège, Allée du 6 août 19, Liège, 4000, Belgium
[7] Department of Earth, Atmospheric and Planetary Science, Massachusetts Institute of Technology, 77 Massachusetts Avenue, Cambridge, MA 02139, USA
[8] Instituto de Astrofísica de Canarias (IAC), Calle Vía Láctea s/n, 38200, La Laguna, Tenerife, Spain
[9] Center for Astrophysics—Harvard & Smithsonian, 60 Garden Street, Cambridge, MA 02138, USA
[10] NASA Exoplanet Science Institute-Caltech/IPAC, Pasadena, CA 91125, USA
[11] Centre for Exoplanet Science, SUPA, School of Physics and Astronomy, University of St Andrews, St Andrews KY16 9SS, UK
[12] Department of Astrophysical Sciences, Princeton University, 4 Ivy Lane, Princeton, NJ 08544, USA
[13] Astrophysics Group, Keele University, Staffordshire ST5 5BG, UK
[14] NASA Ames Research Center, Moffett Field, CA 94035, USA
[15] Observatoire de Genève, Départment d'Astronomie, Université de Genève, Versoix, Switzerland
[16] Department of Physics, University of Warwick, Gibbet Hill Road, Coventry CV 4 7AL, UK
[17] Centre for Exoplanets and Habitability, University of Warwick, Gibbet Hill Road, Coventry CV 4 7AL, UK
[18] Department of Astronomy, Wellesley College, Wellesley, MA 02481, USA
[19] Departamento de Astrofísica, Universidad de La Laguna, E-38206 La Laguna, Tenerife, Spain
[20] Brierfield Observatory Bowral, NSW 2576, Australia
[21] Astronomy & Astrophysics Division, Physical Research Laboratory, Ahmedabad 380009, India
[22] Department of Physics, Indian Institute of Technology, 382335 Gandhinagar, India
[23] Instituto de Astrofísicae Ciências do Espaço, Universidade do Porto, CAUP, Rua das Estrelas, 4150-762 Porto, Portugal
[24] Lomonosov Moscow State University, Sternberg Astronomical Institute, Universitetsky pr., 13, 119992, Moscow, Russian Federation
[25] Jet Propulsion Laboratory, California Institute of Technology, Pasadena, CA 91109, USA
[26] Space Sciences, Technologies and Astrophysics Research (STAR) Institute, Université de Liège, Allée du 6 Août 19C, B-4000 Liège, Belgium
[27] Institute of Astronomy, KU Leuven, Celestijnenlaan 200D, 3001 Leuven, Belgium
[28] International Center for Advanced Studies (ICAS) and ICIFI (CONICET), ECyT-UNSAM, Campus Miguelete, 25 de Mayo y Francia, (1650) Buenos Aires, Argentina
[29] Division of Plastic Surgery, Department of Surgery, University of California, Los Angeles, CA, USA
[30] NSF's National Optical-Infrared Astronomy Research Laboratory, 950 N. Cherry Avenue, Tucson, AZ 85719, USA
[31] Komaba Institute for Science, The University of Tokyo, 3-8-1 Komaba, Meguro, Tokyo 153-8902, Japan; afukui@g.ecc.u-tokyo.ac.jp, narita@g.ecc.u-tokyo.ac.jp
[32] Instituto de Astrofísica de Canarias (IAC), E-38205 La Laguna, Tenerife, Spain; fmurgas@iac.es, epalle@iac.es
[33] Center for Space Sciences and Technology, University of Maryland, Baltimore County, Baltimore, MD 21250, USA
[34] LESIA, Observatoire de Paris, Université PSL, CNRS, Sorbonne Université, Université de Paris, 5 place Jules Janssen, 92195 Meudon, France
[35] Société Astronomique de France, 3 Rue Beethoven, 75016 Paris, France
[36] Astrobiology Center, 2-21-1 Osawa, Mitaka, Tokyo 181-8588, Japan; john.livingston@nao.ac.jp
[37] National Astronomical Observatory of Japan, 2-21-1 Osawa, Mitaka, Tokyo 181-8588, Japan
[38] Astronomical Science Program, Graduate University for Advanced Studies, SOKENDAI, 2-21-1, Osawa, Mitaka, Tokyo, 181-8588, Japan
[39] Institut d'Astrophysique et de Géophysique, Université de Liége, 17 Allée du 6 Août, Bat. B5C, 4000 Liège, Belgium
[40] Department of Physics and Astronomy, University of New Mexico, 1919 Lomas Boulevard NE, Albuquerque, NM 87131, USA
[41] Departamento de Astrofísica, Universidad de La Laguna (ULL), E-38206 La Laguna, Tenerife, Spain
[42] Institute for Astronomy, University of Edinburgh, Edinburgh, UK
[43] Astronomy & Astrophysics Group, Department of Physics, University of Warwick, Gibbet Hill Road, Coventry CV 4 7AL, UK

*Received 2024 December 13; revised 2025 March 31; accepted 2025 April 7; published 2025 May 27*

---

[44] NASA Postdoctoral Program Fellow.

## Abstract

The Wide Angle Search for Planets (WASP) survey provided some of the first transiting hot Jupiter candidates. With the addition of the Transiting Exoplanet Survey Satellite (TESS), many WASP planet candidates have now been revisited and given updated transit parameters. Here, we present nine transiting planets orbiting FGK stars that were identified as candidates by the WASP survey and found to have planetary masses via radial velocity measurements. Subsequent space-based photometry taken by TESS as well as ground-based photometric and spectroscopic measurements have been used to jointly analyze the planetary properties of WASP-102 b, WASP-116 b, WASP-149 b WASP-154 b, WASP-155 b, WASP-188 b, WASP-194 b/HAT-P-71 b, WASP-195 b, and WASP-197 b. These planets have radii between 0.9 $R_{\rm Jup}$ and 1.4 $R_{\rm Jup}$, masses between 0.1 $M_{\rm Jup}$ and 1.5 $M_{\rm Jup}$, and periods between 1.3 and 6.6 days.

*Unified Astronomy Thesaurus concepts:* Exoplanet systems (484); Hot Jupiters (753); Exoplanets (498)

*Materials only available in the online version of record: figure sets, machine-readable table*

## 1. Introduction

Scorching-hot, massive planets in tight orbits around their stars were once the realm of science fiction. However, by the early 2000s, exoplanet surveys had begun to discover many of these "hot Jupiter" systems. While these planets are comparatively rare, their frequent, deep transits make them accessible to wide-field ground-based surveys. In fact, there are now more than 600 known planets larger than half the radius of Jupiter with orbits under 10 days. Even with a growing sample of these strange planets, their formation history remains a mystery. Did these planets form in their current location, or did they originate farther beyond the snow line and migrate inward to their present location? While observing an individual planet's history is not possible, we can explore the influence of different physical drivers that shape planetary formation and evolution through the careful study of population-level demographics (see J. J. Fortney et al. 2021, for a review).

One early contributor to the sample of hot Jupiter planets was the Wide Angle Search for Planets (WASP) survey (D. L. Pollacco et al. 2006). From locations in the Northern and Southern Hemispheres, the full sky was monitored for stars showing transit dips. While this strategy provides a vast sample of stars to search, it also presents challenges in terms of data processing and follow-up efforts. Due to the combination of systematic noise, scatter, and pixel size leading to blending, many genuine transit signals appear inconclusive, while many false positives are flagged for follow-up. Nonetheless, the WASP survey has led to the discovery of nearly 200 planets, including the actively inspiraling WASP-12 b (L. Hebb et al. 2009; S. W. Yee et al. 2020), the close-in planet orbiting a giant $\delta$-Scuti star WASP-33 b (A. Collier Cameron et al. 2010), and the planet with a tail WASP-69 b (D. R. Anderson et al. 2014; D. Tyler et al. 2024). In the discovery process, WASP has also identified 1041 false positives in the Northern Hemisphere alone (N. Schanche et al. 2019a).

The launch of the Transiting Exoplanet Survey Satellite (TESS; G. R. Ricker et al. 2015) in 2018 April provided an opportunity to better characterize existing planetary systems as well as rule out false alarms due to systematics for the remaining WASP planet candidates, without the need to schedule and coordinate extensive follow-up from the ground. TESS' ∼27 day observing windows, referred to as Sectors, provide longer continuous observing intervals than are possible to achieve from the ground, thereby alleviating the challenge of observing the transits with drifting periods and ephemerides.

In this paper, we present nine planets that (1) were initially identified as candidates in the WASP survey, (2) have sufficient radial velocity follow-up to establish a planetary mass, (3) have not been published in an accepted refereed paper, and (4) have been identified as TESS Objects of Interest (TOIs). These planets fall in the hot Jupiter regime, with periods ranging from 1.3 to 6.6 days and radii roughly that of Jupiter. In Section 2, we highlight the wide array of observations used to characterize the objects, while in Section 3 we describe the methods used to refine the properties of the host stars. Section 4 presents the final models that jointly fit the transit and radial velocity data in order to characterize the planets. Section 5 provides discussion of the new planets in the context of the exoplanet population at large. Finally, we provide a summary of the work in Section 6.

## 2. Observations

All planets reported here were discovered via their transit signals. However, further observations were obtained to establish the planetary interpretation of the data and rule out potential false positives. In this section, we describe the facilities used to obtain photometric (Section 2.1), spectroscopic (Section 2.2), and high-resolution imaging (Section 2.3) data. Many of these contributions were made by collaborators in the TESS Follow-up Observing Program (TFOP).

### *2.1. Photometry*

All planets presented here were originally identified as transit candidates in WASP data. In addition, TESS observed each star for one or more sectors. A variety of additional ground-based data were taken to further constrain the transit timing and depth, and when possible, to confirm that a consistent planet–star radius ratio is measured at different wavelengths in order to exclude eclipsing binary systems. A full description of the photometric data available for each star can be found in Tables 1 (TESS) and 2 (ground facilities). Additional information on the observation of each target can be found in Section 4.

### *2.1.1. WASP*

With regular operations starting in 2006, WASP was among the first ground-based surveys dedicated to searching for exoplanets via the transit method. To achieve a large sky coverage, the WASP consortium consists of instruments at two observatory sites. The northern skies are surveyed by SuperWASP, located at the Observatorio del Roque de los Muchachos on La Palma, while the southern skies are probed by WASP-South at the Sutherland station of the South African Astronomical Observatory (SAAO). The telescopes at each site

**Table 1**
Summary of TESS Observations Used for Analysis

| Target | Sector | Cadence (s) | Source |
|---|---|---|---|
| WASP-102/TOI-6170 | 56 | 200 | TESS-SPOC |
| WASP-116/TOI-4672 | 31 | 600 | TESS-SPOC |
| WASP-149/TOI-6101 | 61 | 120 | SPOC |
| WASP-154/TOI-5288 | 42 | 600 | TESS-SPOC |
| WASP-155/TOI-6135 | 56 | 200 | QLP |
| WASP-188/TOI-5190 | 40, 53, 54 | 200 | TESS-SPOC |
| WASP-194/HAT-P-71/TOI-3791 | 40, 41, 50, 54, 55, 56, 57, 60 | 120 | SPOC |
| WASP-195/TOI-4056 | 50, 52 | 120 | SPOC |
| WASP-197/TOI-5385 | 48 | 120 | SPOC |

**Notes.** When possible, 120 s PDCSAP lightcurves produced by the TESS pipeline were used (J. C. Smith et al. 2012; M. C. Stumpe et al. 2012, 2014). When the star was observed only in FFIs, lightcurves produced by the High-Level Science Products TESS-SPOC or QLP were used, as indicated in the table.

are composed of eight commercial camera lenses (Canon 200 mm $f/1.8$) with 2k x 2k E2V CCD cameras.

Once WASP data are collected, images are processed to provide lightcurves for all stars in the field. In this study, we use the ORion transit search Combining All data on a given target with the TAMuz and Trend Filtering Algorithm (TFA) decorrelation (ORCA_TAMTFA) product, which, as the lengthy name suggests, removes common patterns of systematic error using a combination of the TFA (G. Kovács et al. 2005) and the SysRem algorithm (O. Tamuz et al. 2005). A box-least-squares (BLS; G. Kovács et al. 2002) method is then applied to search for transit signals in the detrended lightcurves. Originally, all candidates were searched for by eye, but later a machine-learning model was applied to the lightcurves (N. Schanche et al. 2019b), which highlighted the candidates WASP-194 b, WASP-195 b, and WASP-197 b as strong candidates for further characterization.

### *2.1.2. TESS*

TESS, launched in April of 2018, is a space-based all-sky survey with a primary goal to search for exoplanet transits around nearby, bright stars. TESS' four broadband, red-sensitive cameras stare at a $24° \times 90°$ strip of the sky in 27 day blocks, called Sectors. The spacecraft then reorients itself to point at another patch of sky. In the 6 yr since launch, TESS has surveyed more than 95% of the sky, and it will continue to fill in the remaining observational gaps in future Sectors.

This observing strategy makes TESS a great compliment to WASP's legacy. For WASP targets already characterized by existing follow-up observations, the new TESS observations help to refine the orbital parameters of the system. For the candidates that still require additional observations, TESS' near-all-sky coverage provides the ability to quickly search for corresponding transit signals and identify astrophysical or systematic false alarms.

The nine planetary systems presented in this paper were flagged as planet candidates in the WASP data archive and were also independently identified as TOIs by the TESS Science Office (N. M. Guerrero et al. 2021). Four of the stars have "postage stamp" data from TESS, meaning that 120 s cadence, systematic error-corrected lightcurves produced by the Science Processing Operations Center (SPOC; J. M. Jenkins et al. 2016) are available. The remaining five stars were observed in the TESS full-frame images (FFIs) with a cadence of 1800 s (primary mission), 600 s (first mission extension), or 200 s (second mission extension). While the SPOC did not automatically extract lightcurves for these five stars, there are a number of community-created High-Level Science Products (HLSPs) available that produce detrended lightcurves from FFI data. In this work, we use lightcurves produced by either the Quick-Look Pipeline (QLP; C. X. Huang et al. 2020a, 2020b; M. Kunimoto et al. 2022) or the TESS-SPOC (D. A. Caldwell et al. 2020) HLSPs, which are available at MAST (See Table 1). When FFI lightcurves were available with multiple cadences, we chose to use only sectors with the shortest cadence available.

### *2.1.3. HATNet*

WASP-194/HAT-P-71 b was independently identified as a candidate transiting planet system by the Hungarian-made Automated Telescope Network (HATNet) project (G. Bakos et al. 2004) based on time-series observations gathered by all six of the instruments in the network. Four of these instruments are located at Fred Lawrence Whipple Observatory in Arizona, while the other two are located at Maunakea Observatory in Hawaii.

The star was observed in two separate HATNet fields: G081 and G115. A total of 11,124 observations of WASP-194/HAT-P-71 in field G081 were gathered through a Sloan $r'$ filter between 2012 July 20 and 2012 December 20 using an exposure time of 3 minutes. Field G115 was observed using both a Cousins $R_C$ filter and a Sloan $r'$ filter. A total of 2298 $R_C$ observations were obtained between 2008 August 6 and 2008 September 14 using an exposure time of 5 minutes, while 7141 $r'$ observations were obtained between 2008 September 15 and 2010 July 25 using an exposure time of 3 minutes. The G081 $r'$, G115 $R_C$, and G115 $r'$ observations were independently reduced to aperture photometry lightcurves following the procedure described by G. A. Bakos et al. (2010). Instrumental systematic variations were removed from the lightcurves using TFA, and the lightcurves were searched for transiting planet signals using the BLS algorithm. Following this process, WASP-194/HAT-P-71/TOI-3791b was identified as a transiting planet candidate system on 2013 October 7, and follow-up observations were carried out to establish the planetary nature of the system.

### *2.1.4. NITES*

We observed a transit of WASP-154 b on 2016 August 8 and a transit of WASP-155 b on 2016 August 11 using the Near Infrared Transiting ExoplanetS telescope (NITES; J. McCormac et al. 2014) located in La Palma. A total of 525 30 s cadence images were obtained for WASP-154 b using an *I*-band filter, and 604 30 s images of WASP-155 b were obtained using an *R*-band filter. The data were reduced in PYTHON using CCDPROC (M. W. Craig et al. 2015). A master bias, dark, and flat were created using the standard process on each night. A minimum of

**Table 2**
Summary of Ground-based Photometric Time-series Observations for the Nine Planets

| Target | Filter | Facility | Date | Transit Coverage |
|---|---|---|---|---|
| WASP-102/TOI-6170 | Broadband | WASP | 2009-07-14–2011-11-10 | ⋯ |
| ⋯ | Blue-blocking | TRAPPIST | 2013-08-13 | Full |
| ⋯ | $r$-Gunn | EulerCam | 2013-08-13 | Full |
| ⋯ | Blue-blocking | TRAPPIST | 2013-09-20 | Full |
| ⋯ | $I_{\rm C}$ | EulerCam | 2013-09-20 | Full |
| ⋯ | Blue-blocking | TRAPPIST | 2013-10-09 | Full |
| WASP-116/TOI-4672 | Broadband | WASP | 2008-07-30–2010-12-27 | ⋯ |
| ⋯ | Blue-blocking | TRAPPIST | 2013-11-05 | Ingress |
| ⋯ | NGTS | EulerCam | 2013-11-05 | Ingress |
| ⋯ | Blue-blocking | TRAPPIST | 2013-11-25 | Ingress |
| ⋯ | NGTS | EulerCam | 2013-11-25 | Ingress |
| ⋯ | SDSS $i'$ | LCO/SAAO | 2023-10-15 | Ingress |
| ⋯ | SDSS $i'$ | LCO/HAL | 2023-10-22 | Ingress |
| WASP-149/TOI-6101 | Broadband | WASP | 2009-11-20–2012-03-31 | ⋯ |
| ⋯ | Sloan $z'$ | TRAPPIST | 2015-02-06 | Full |
| ⋯ | $z$-Gunn | EulerCam | 2015-04-07 | Full |
| ⋯ | Sloan $z'$ | TRAPPIST | 2015-05-05 | Full |
| ⋯ | Sloan $z'$ | TRAPPIST | 2015-11-26 | Full |
| ⋯ | $z$-Gunn | EulerCam | 2015-12-20 | Full |
| WASP-154/TOI-5288 | Broadband | WASP | 2008-06-06–2010-10-28 | ⋯ |
| ⋯ | NGTS | EulerCam | 2016-08-04 | Full |
| ⋯ | $I$ | NITES | 2016-08-08 | Full |
| ⋯ | Blue-blocking | TRAPPIST | 2015-10-08 | Full |
| ⋯ | Sloan $z'$ | TRAPPIST | 2017-07-13 | Full |
| ⋯ | SDSS $i'$ | LCO/CTIO | 2022-06-21 | Full |
| ⋯ | $R$ | Brierfield | 2022-06-13 | Full |
| WASP-155/TOI-6135 | Broadband | WASP | 2004-05-25–2007-11-22 | ⋯ |
| ⋯ | None | NITES | 2016-08-11 | Full |
| ⋯ | $g'$, $r'$, $zs$ | MuSCAT2 | 2019-08-18 | Full |
| WASP-188/TOI-5190 | Broadband | WASP | 2004-05-14–2010-08-24 | ⋯ |
| ⋯ | $g'$, $r'$, $i'$, $zs$ | MuSCAT2 | 2018-06-10 | Ingress |
| ⋯ | Sloan $i'$ | KeplerCam | 2022-04-25 | Egress |
| WASP-194/HAT-P-71/TOI-3791 | Broadband | WASP | 2007-05-10–2010-09-22 | ⋯ |
| ⋯ | Sloan $r'$, Cousins $R_{\rm C}$ | HATNet | 2008-08-06–2012-12-20 | ⋯ |
| ⋯ | CBB | OPM | 2021-07-04 | Full |
| ⋯ | $g'$, $r'$, $i'$, $zs$ | MuSCAT2 | 2021-07-04 | Full |
| ⋯ | Sloan $i'$ | KeplerCam | 2017-05-24 | Full |
| WASP-195/TOI-4056 | Broadband | WASP | 2007-03-30–2011-08-04 | ⋯ |
| ⋯ | Sloan $r'$ | Whitin | 2022-06-06 | Full |
| WASP-197/TOI-5385 | Broadband | WASP | 2006-12-22–2007-05-05 | ⋯ |

**Note.** See text for further details on these observations.

21 of each frame were used in each master calibration frame. Nonvariable nearby comparison stars were selected by hand and aperture photometry was extracted using SEP (E. Bertin & S. Arnouts 1996; K. Barbary et al. 2016). The shift between each image was measured using the DONUTS algorithm (J. McCormac et al. 2013), and the photometry apertures were recentered.

### 2.1.5. MuSCAT2

We observed WASP-155 b, WASP-188 b, and WASP-194 b using the MuSCAT2 multicolor imager (N. Narita et al. 2019) installed on the 1.52 m Telescopio Carlos Sánchez (TCS) at the Teide Observatory in Tenerife, Spain. MuSCAT2 is a four-color simultaneous imager with four e2v 1024 × 1024 pixel CCD detectors, providing a $7\overset{\prime}{.}4 \times 7\overset{\prime}{.}4$ field-of-view and a pixel scale of $0\overset{\prime\prime}{.}43$ px$^{-1}$.

A partial transit of WASP-188 b was observed on 2018 June 10, a full transit of WASP-155 b was observed on 2019 August 18, and a full transit of WASP-194 b was observed on 2021 July 4. The observing conditions were generally good for all the observations; however, some of the WASP-194 data had to be discarded due to saturation. The exposure times were optimized separately for each night and camera.

A dedicated MuSCAT2 photometry pipeline (H. Parviainen et al. 2019) was used to perform standard reduction steps and aperture photometry. The pipeline calculates aperture photometry for various aperture sizes and comparison stars, generating the final relative lightcurves via global optimization of the photometry and a transit model calculated using PyTransit (H. Parviainen 2015).

### 2.1.6. KeplerCam

WASP-194/HAT-P-71 was observed through a Sloan $i'$ filter with the KeplerCam imager on the Fred Lawrence Whipple Observatory (FLWO) 1.2 m telescope on the following eight nights: 2014 October 5, 2015 April 17, 2016 April 20, 2016 April 28, 2016 October 6, 2016 October 22, 2017 April 18, and 2017 May 23. The observations were gathered with an exposure time of 13 s, and the telescope was kept in focus. The data were reduced to ensemble-corrected aperture photometry lightcurves following the procedures described in G. A. Bakos et al. (2010). The observations on the first two nights were fully out of transit, and were used to refine the transit ephemeris. The observations on 2016 October 6 were cut short due to weather, so only out-of-transit observations were gathered. An ingress was observed on 2016 April 20, and egresses were observed on 2016 April 28, 2016 October 22, and 2017 April 18. Finally, a full transit was observed on 2017 May 23, and we include only this transit in our final analysis of the system.

An egress of WASP-188/TOI-5190b was observed with the KeplerCam instrument on the night of 2022 April 25 using a Sloan $i'$ filter. A total of 442 observations were collected at an average cadence of 34 s. The images were calibrated, and aperture photometry was extracted for the target, as well as for a number of comparison stars, using the AstroImageJ package (K. A. Collins et al. 2017). We used a 5 pixel radius aperture, corresponding to $3\overset{''}{.}36$, for the photometry.

### 2.1.7. TRAPPIST-South

The TRAnsiting Planets and PlanetesImals Small Telescope (TRAPPIST; M. Gillon et al. 2011; E. Jehin et al. 2011), located at ESA's La Silla Observatory in Chile observed four of the transiting planets here. The telescope has an FLI camera with an image scale of $0\overset{''}{.}64$ px$^{-1}$, and is fitted with several optical filters, including the blue-blocking filter that has a transmittance >90% from 500 to above 1000 nm. The image data were extracted via the dedicated pipeline.

The transits of WASP-102 b, WASP-116 b, and WASP-154 b were observed using this blue-blocking filter with exposure times of 22, 11, and 9 s, respectively. The transits of WASP-149 b were observed using the Sloan $z'$ filter with exposures of either 10 or 13 s.

### 2.1.8. EulerCam

We used EulerCam at the 1.2 m Euler telescope located at La Silla observatory to observe transits of WASP-102 b, WASP-116 b, WASP-149 b, and WASP-154 b. The instrument is a back-illuminated 4k × 4k CCD imager, with a pixel resolution of $0\overset{''}{.}215$ px$^{-1}$ and a field of view of $14\overset{'}{.}76 \times 14\overset{'}{.}76$. For all observations, photometry was extracted via differential aperture photometry, optimizing aperture size and reference stars iteratively to achieve minimal residual rms on the final transit lightcurve. The instrument and associated data reduction procedures are described in detail in M. Lendl et al. (2012).

WASP-102 was observed throughout two full transits of planet b on 2013 August 13 and 2013 September 20 using an $r$-Gunn and an $I$-Cousins filter, respectively. Two partial transits of WASP-116 were observed on 2013 November 05 and 2013 November 25 through a broad NGTS filter (500–900 nm), while applying a defocus of 0.15 mm to optimize the duty cycle. Two full transits of WASP-149 b were observed through a $z$-Gunn filter on 2015 April 7 and 2015 December 20, and a full transit of WASP-154 b was observed through a NGTS filter on 2016 August 4, again applying a 0.1 mm defocus.

### 2.1.9. LCOGT

The Las Cumbres Observatory Global Telescope network (LCOGT; T. M. Brown et al. 2013) is a globally distributed network of 0.4, 1, and 2 m telescopes. We make use of observations from three of the network telescopes as described below.

WASP-116 b was observed on 2023 October 15 by the 0.35 m telescope at the SAAO and again on 2023 October 22 by the 0.35 m telescope at Halaeakala (HAL), both using the $i'$ filter. Both observations showed an on-time transit consistent with the expected depth.

We observed a full transit of WASP-154 b on 2022 June 21 from the LCOGT 0.4 m network node at Cerro Tololo Inter-American Observatory (CTIO). The telescope is equipped with 2048 × 3072 SBIG STX6303 cameras having a pixel scale of $0\overset{''}{.}57$ px$^{-1}$, resulting in a $19' \times 29'$ field of view. The observation was carried out in the $i'$ filter with an exposure time of 180 s. The science-image calibration was performed using the standard LCOGT BANZAI pipeline (C. McCully et al. 2018), and photometric extraction was performed using AstroImageJ (K. A. Collins et al. 2017). Some data were affected because of the poor sky transparency.

### 2.1.10. Brierfield Private Observatory

The Brierfield Observatory is located near Bowral, N.S.W. Australia. The 0.36 m Planewave CDK14 telescope is equipped with a 4096 × 4096 Moravian 16 803 camera. The image scale after binning 2 × 2 is $1\overset{''}{.}47$ px$^{-1}$, resulting in a $50' \times 50'$ field of view. The photometric data for WASP-154 includes a single full transit with the $R_C$ filter, consisting of 120 200 s exposures extracted on 2022 June 13 using the `AstroImageJ` software package (K. A. Collins et al. 2017), utilizing a circular photometric aperture with an $11\overset{''}{.}8$ radius and no detrending parameters.

### 2.1.11. Whitin

We observed a transit of WASP-195 b as part of the TFOP program on 2022 June 6 using the Whitin Observatory 0.7 m PlaneWave telescope in Eastern Massachusetts, USA. Its FLI ProLine PL23042 CCD camera has a pixel scale of $0\overset{''}{.}68$ px$^{-1}$, resulting in a $23' \times 23'$ field of view. We collected 350 exposures of length 30 s with a Sloan $r'$ filter, with a gap due to clouds. We used `AstroImageJ` (K. A. Collins et al. 2017) to perform standard calibration and photometric extraction in a $5\overset{''}{.}4$ radius circular aperture.

### 2.1.12. Observatoire Privé du Mont

The transit of WASP-194 b was observed by the Observatoire Privé du Mont (OPM), located in Saint-Pierre du Mont. The facility hosts a Ritchey-Chrétien GSO 0.2 m telescope with an Atik 383L+ camera. A full transit was observed on 2021 July 4 using a CBB filter. The lightcurve was extracted using a $2\overset{''}{.}2$ aperture.

## 2.2. Spectroscopy

All nine planets presented here have masses characterized through radial velocity (RV) measurements. Below, we briefly describe these facilities and observations. A summary of the observations can be found in Table 3.

**Table 3**
Summary of Radial Velocity Observations Used to Characterize the Planet Masses

| Target | Facility | $N_{\rm obs}$ | Observation Span |
|---|---|---|---|
| WASP-102/TOI-6170 | SOPHIE | 14 | 2012 Sept–2013 Jan |
| … | CORALIE | 11 | 2013 Sept–2014 Aug |
| WASP-116/TOI-4672 | SOPHIE | 15 | 2013 Jan–2013 Nov |
| … | CORALIE | 24 | 2013 Aug–2014 Nov |
| WASP-149/TOI-6101 | SOPHIE | 15 | 2014 Nov–2015 Apr |
| … | CORALIE | 11 | 2013 Dec–2015 Apr |
| WASP-154/TOI-5288 | SOPHIE | 14 | 2014 Nov–2015 Oct |
| WASP-155/TOI-6135 | SOPHIE | 22 | 2015 Jul–2015 Dec |
| WASP-188/TOI-5190 | SOPHIE | 15 | 2015 Jul–2015 Dec |
| WASP-194/HAT-P-71/ TOI-3791 | FLWO/TRES | 29 | 2013 Oct–2016 Sept |
| WASP-195/TOI-4056 | SOPHIE | 88 | 2014 May–2021 Jul |
| WASP-197/TOI-5385 | FLWO/TRES | 16 | 2022 Apr–2024 Apr |
| … | SOPHIE | 5 | 2023 Feb–2024 Jan |
| … | PARAS-2 | 8 | 2024 Jan–2024 Mar |

### 2.2.1. SOPHIE

Between 2014 and 2024, we observed eight of the nine objects presented here with the SOPHIE spectrograph at the 193 cm telescope at Observatoire de Haute-Provence, France. This is a stabilized échelle spectrograph dedicated to high-precision radial velocity measurements in optical wavelengths (S. Perruchot et al. 2008; F. Bouchy et al. 2009). We used its high-efficiency mode (resolving power $R = 40{,}000$) and the slow-reading mode of its CCD for seven of them (WASP-102, 116, 149, 154, 155, 188, and 195). WASP-197 was observed with SOPHIE's high-resolution mode ($R = 75{,}000$) and the fast-reading mode. Depending on the stars and the weather conditions, exposure times typically range between 15 and 45 minutes, for typical signal-to-noise ratios per pixel at 550 nm between 20 and 50. A few exposures with particularly low signal-to-noise ratios were excluded.

The radial velocities were extracted with the SOPHIE pipeline, as presented by F. Bouchy et al. (2009) and refined by N. Heidari et al. (2024), who derives cross-correlation functions (CCF) from standard numerical masks corresponding to different spectral types. In particular, that version of the pipeline includes corrections for CCD charge-transfer inefficiency, instrumental drifts, and pollution by moonlight. Moonlight is estimated and corrected using the second SOPHIE fiber aperture that is targeted on the sky, 2′ away from the first one pointing toward the star.

The derived radial velocities and their uncertainties are available through the Digital Repository for the University of Maryland (DRUM).[45] They show variations in phase with the periods and transit times derived from photometry. The amplitudes of those radial velocity variations agree with planetary masses, and they do not depend on the stellar type of the numerical mask used for the CCF, as it might be expected in cases where photometric transits are actually caused by blended binary stars of different spectral types. In addition, the bisector spans measured on the CCF show no significant variations nor correlations with the observed radial velocity variations, as it might also be expected in cases of blended eclipsing binaries perturbing the profiles of the spectral lines (D. Queloz et al. 2001).

Thus, those measurements establish the planetary nature of the transiting events, and they constrain the mass of the transiting planets as well as the eccentricity of their orbits.

### 2.2.2. FLWO/TRES

The Tillinghast Reflector Echelle Spectrograph (TRES; G. Furész 2008) was used to obtain reconnaissance spectra of WASP-197 and WASP-194. TRES is is a fiber-fed echelle spectrograph with a wavelength range of 390–910 nm and a resolving power of $R \approx 44{,}000$ mounted on the 1.5 m Tillinghast Reflector telescope at the Fred Lawrence Whipple Observatory (FLWO) atop Mount Hopkins, Arizona. Thirty spectra of WASP-197 were obtained during 2013 October and 2016 September, and 16 spectra of WASP-194 during 2022 April and 2024 April. The spectra were extracted as described in L. A. Buchhave et al. (2010), and a multiorder analysis was used to derive RVs. The multiorder analysis uses the strongest observed spectrum as a template and then cross-correlates each spectrum, order-by-order, against the template spectrum.

For the TRES observation of WASP-194, there was a single outlying data point of several hundred meters per second. This data point corresponded to an observation during a full moon, which could likely have contaminated the observation. We therefore remove this data point from analysis.

### 2.2.3. CORALIE

The high-resolution CORALIE spectrograph (D. Queloz et al. 2000) is installed at the 1.2 m Leonhard Euler Telescope at ESO's La Silla Observatory in Chile. Eleven observations of WASP-102 were taken by CORALIE between 2012 and 2014, all obtained during gray/dark time to reduce stray light from the moon. WASP-116 was observed by CORALIE on 24 nights. However, one of these observations was taken after the optical fiber of CORALIE was replaced in November of 2014. We therefore exclude the last data point from our analysis. Similarly, 9 of the 11 CORALIE data points for WASP-149 were taken after the optical fiber change. We use only these nine data points in our final analysis.

### 2.2.4. PARAS-2

RV follow-up of WASP-197 was done with the PARAS-2 spectrograph. The spectrograph is attached to the PRL 2.5 m telescope at Mount Abu Observatory and works at high resolution ($R \approx 107{,}000$) in 380–690 nm. It uses the simultaneous referencing method using the uranium argon (UAr) hollow cathode lamp for wavelength calibration and precise RV calculations. More details of the spectrograph can be found in A. Chakraborty et al. (2018, 2024).

A total of eight spectra were acquired between 2024 January 4 and April 8. The exposure time of each exposure was kept at 60 minutes, which resulted in a signal-to-noise ratio of 18–30 per pixel at a blaze peak wavelength of 550 nm. A custom-made PARAS-2 pipeline is used for data extraction and RV calculations (S. Baliwal et al. 2024). In brief, before doing the optimal extraction of the spectra, the pipeline does various corrections, including bias and dark subtractions, cosmic-ray rejection, scattered light corrections etc. The pipeline is written in IDL and based upon the PARAS-1 pipeline (A. Chakraborty et al. 2014) and the algorithms of N. E. Piskunov & J. A. Valenti (2002). The RVs are calculated by cross-correlating the extracted and wavelength-calibrated spectra with a template spectrum of

---

[45] 10.13016/iuro-f0od

**Table 4**
Summary of the Identified Nearby (< 10″) Stellar Companions to the Planet-hosting Stars

| Primary Target | Nearby Companion Gaia ID | Δmag (Filter) | Distance (arcsec) |
|---|---|---|---|
| WASP-149 | 3062565055054980352 | 9.0 (G) | 7.8 |
| WASP-154 | 2618260274649763840 | 8.4 (G) | 5.3 |
| WASP-155 | 1910906408272899200 | 2.6 (G), 5.3[a] (832 nm) | 2.9 |
| … | 1910906403977533184 | 6.4 (G) | 8.3 |
| WASP-188 | 2095929373136748928 | 5.7 (G), 5.5 (I) | 1.8 |
| … | 2095930850605499136 | 5.2 (G) | 4.1 |
| WASP-194 | 2139082485811741440 | 0.5 (G) | 9.7 |
| WASP-197 | 734156214654777984 | 6.5 (G) | 6.7 |

**Note.**
[a] See Section 4.0.5.

G-type stars. The RV photon noise is found to be between 8.3 and 18.4 m s$^{-1}$, calculated using the techniques mentioned in P. Chaturvedi et al. (2016).

### 2.3. High-resolution Imaging

Close stellar companions (bound or line-of-sight) can confound exoplanet discoveries in a number of ways. The detected transit signal might be a false positive due to a background eclipsing binary. Even real planet discoveries will yield incorrect stellar and exoplanet parameters if a close companion exists and is unaccounted for (D. R. Ciardi et al. 2015; E. Furlan et al. 2017). Additionally, the presence of a close companion star leads to the nondetection of small planets residing within the same exoplanetary system (K. V. Lester et al. 2021). Given that nearly one half of solar-like stars are in binary or multiple-star systems (R. A. Matson et al. 2018), high-resolution imaging provides crucial information toward our understanding of exoplanetary formation, dynamics and evolution.

The high-resolution imaging used in this work is presented below. Plots showing a selection of the contrast curves can be found in Appendix C. We summarize the nearby (<10″) companions identified in Table 4.

#### 2.3.1. WIYN/NESSI

The stars WASP-116, WASP-155, WASP-194, WASP-195, and WASP-197 were observed using the NN-EXPLORE Exoplanet Stellar Speckle Imager (NESSI; N. J. Scott et al. 2018), a speckle imager employed at the WIYN 3.5 m telescope on Kitt Peak, Arizona. NESSI is a dual-channel speckle imager that yields simultaneous speckle images in two filters. WASP-116, WASP-155, and WASP-194 were observed on 2023 January 28, and WASP-155 and WASP-194 were both observed on 2024 September 12 through two filters centered at $\lambda_c$ = 562 nm and 832 nm. WASP-195 and WASP-197 were observed on 2022 April 21 and April 18 respectively, using only the 832 nm filter due to an alignment problem with the blue channel during this time. Each observation consisted of a set of nine 1000 frame 40 ms speckle exposures. The field of view was set by the subarray readout region of 256 × 256 pixels to be 4″.6 × 4″.6 arcsec, although speckle measurements are limited to a smaller radial extent from the target star. Alongside the observation of the science target, a single 1000 frame image set was taken of a nearby single star (point source) for calibration of the underlying PSF.

The speckle data were reduced using the pipeline described in S. B. Howell et al. (2011). The pipeline produces, among other things, a reconstructed image of the field around each target and a contrast curve representing the relative magnitude limits for detecting nearby point sources between the diffraction-limited inner working angle (0″.04–0″.06 for these filters) and an outer angle of 1″.2. No companion sources were detected within 1″.2 of any of the targets in the NESSI data, the angular extent over which the speckle data are most accurate. In the case of WASP-155, we tentatively report a star 2″.9 from the target. More information about this companion can be found in Section 4.0.5.

#### 2.3.2. SAI/Speckle Polarimeter

WASP-188 was observed on 2023 December 2, and WASP-197 was observed two nights later with the speckle polarimeter on the 2.5 m telescope at the Caucasian Observatory of Sternberg Astronomical Institute (SAI) of Lomonosov Moscow State University. A low-noise CMOS detector, the Hamamatsu ORCA-quest (I. A. Strakhov et al. 2023), was used as a detector. WASP-195 was observed on 2021 July 20 with a previous, EMCCD-based version of the instrument. The atmospheric dispersion compensator was active, which allowed the $I_c$ band to be used. The corresponding angular resolution is 0″.083. For WASP-188 and WASP-197, we have accumulated 5200 frames with 23 ms exposure. For WASP-195, 4000 30 ms frames were accumulated.

For WASP-195, we did not detect any stellar companions, with detection limits of $\Delta I_c = 4.7$ mag and 6.0 mag at distances 0.25 and 1″.0 from the star, respectively. The SAI observations of WASP-197 provided the detection limits of $\Delta I_c = 4.0$ mag and $\Delta I_c = 5.9$ mag at distances 0.25 and 1″.0 from the star, respectively.

For WASP-188 a companion was detected with a position and magnitude difference consistent with Gaia DR3 2095929373136748928—a star that is $\Delta G = 5.6$ fainter than WASP-188 (=Gaia DR3 2095929368839731072). No other, closer companions were detected with the limits $\Delta I_c = 3.2$ mag and 5.6 mag at distances 0.25 and 1″.0 from the star, respectively.

#### 2.3.3. SOAR/HRCam

We searched for stellar companions to WASP-154, WASP-149, and WASP-102 with speckle imaging on the 4.1 m Southern Astrophysical Research (SOAR) telescope (A. Tokovinin 2018), observing in Cousins $I$-band, a visible bandpass similar to that of TESS. Observations were performed on 2022 February 22 (WASP-154), 2024 January 8 (WASP-149), and 2023 August 31 (WASP-102). More details of the speckle observations from the SOAR TESS survey are available in C. Ziegler et al. (2020). No nearby stars were detected within 3″ of WASP-102, WASP-149, or WASP-154.

#### 2.3.4. Gemini/Alopeke and Zorro

The Alopeke and Zorro instruments are identical speckle imagers located on the Gemini-North and Gemini-South telescopes, respectively (N. J. Scott et al. 2021).[46] The instruments

---

[46] https://www.gemini.edu/sciops/instruments/alopeke-zorro/.

provide simultaneous speckle imaging in two bands (562 nm and 832 nm) with output data products including a reconstructed image and robust contrast limits on companion detections (S. B. Howell et al. 2011).

WASP-116 was observed on 2023 January 09 using the Zorro speckle instrument. The two 5$\sigma$ contrast curves result, and our reconstructed 862 nm speckle image show that WASP-116 is a single star with no close companion brighter than 5–7 mag from the diffraction limit (20 mas) out to $1\farcs2$. At the distance of WASP-116 ($d = 560$ pc), these angular limits correspond to spatial limits of 11–672 au. Alopeke was used to observe WASP-155 on 2024 August 13. The resulting contrast curve showed no companions with a contrast within 5 mag (562 nm) or 6 mag (832 nm) from the diffraction limit out to $1\farcs2$, corresponding to 8–480 au.

### 2.4. Palomar/PHARO

Observations of WASP-197 were made on 2024 February 17 with the PHARO instrument (T. L. Hayward et al. 2001) on the Palomar Hale 5 m telescope in the narrowband $K$-cont filter ($\lambda_o = 2.29$; $\Delta\lambda = 0.035$ $\mu$m) and the $H$-cont filter ($\lambda_o = 1.668$; $\Delta\lambda = 0.018$ $\mu$m) using the P3K natural guide star AO system (R. Dekany et al. 2013). The PHARO pixel scale is $0\farcs025$ px$^{-1}$. A standard five-point quincunx dither pattern with steps of $5''$ was performed three times, with each repeat separated by $0\farcs5$. The reduced science frames were combined into a single mosaic image with final resolutions of $0\farcs099$ and $0\farcs90$, respectively. The sensitivity of the final combined AO image was determined by injecting simulated sources azimuthally around the primary target every 20° at separations of integer multiples of the central source's FWHM (E. Furlan et al. 2017). The brightness of each injected source was scaled until standard aperture photometry detected it with 5$\sigma$ significance. The final 5$\sigma$ limit at each separation was determined from the average of all of the determined limits at that separation, and the uncertainty on the limit was set by the root mean square dispersion of the azimuthal slices at a given radial distance. The infrared imaging did detect a star within $6''$ of the primary target, but no other close-in stars were found, in agreement with the speckle observations.

## 3. Stellar Properties

TRES spectra were used to derive stellar parameters using the Stellar Parameter Classification tool (SPC; L. A. Buchhave et al. 2012) for all stars, with the exception of WASP-154. SPC cross-correlates each observed spectrum against a grid of synthetic spectra based on Kurucz atmospheric models (R. L. Kurucz 1992) and derives the effective temperature, the surface gravity, the metallicity, and the rotational velocity of the star.

Stellar parameters of WASP-154 were derived from the combined SOPHIE spectra unpolluted by moonlight. We used the ARES+MOOG methodology described, e.g., in (S. G. Sousa et al. 2021), together with ARES[47] (S. G. Sousa et al. 2015), to measure the equivalent widths of iron lines selected following S. G. Sousa et al. (2008). A minimization process is used to find the ionization and excitation equilibrium and converge to the best set of spectroscopic parameters, using a grid of Kurucz model atmospheres (R. L. Kurucz 1993) and the radiative transfer code MOOG (C. A. Sneden 1973).

An analysis of the broadband spectral energy distribution (SED) of each star was performed together with the Gaia DR3 parallax (Gaia Collaboration et al. 2021), in order to determine an empirical measurement of the stellar radii (K. G. Stassun & G. Torres 2016; K. G. Stassun et al. 2017, 2018). Where available, the $JHK_S$ magnitudes were sourced from 2MASS, the W1–W4 magnitudes from WISE, the $G_{\rm BP}G_{\rm RP}$ magnitudes from Gaia, and the NUV magnitude from GALEX. The absolute flux-calibrated Gaia spectrum was also utilized, when available. Together, the available photometry spans the full stellar SED over a wavelength range of at least 0.4–10 $\mu$m and as much as 0.2–20 $\mu$m (see Figure 1).

A fit using PHOENIX stellar atmosphere models (T. O. Husser et al. 2013) was performed, adopting from the spectroscopic analysis the effective temperature ($T_{\rm eff}$), metallicity ([Fe/H]), and surface gravity ($\log g$). The extinction $A_V$ was fitted for, limited to the maximum line-of-sight value from the Galactic dust maps of D. J. Schlegel et al. (1998). Integrating the (unreddened) model SED gives the bolometric flux at Earth, $F_{\rm bol}$. Taking the $F_{\rm bol}$ together with the Gaia parallax directly gives the bolometric luminosity, $L_{\rm bol}$. The Stefan–Boltzmann relation then gives the stellar radius, $R_\star$. In addition, the stellar mass was estimated using the empirical relations of G. Torres et al. (2010). Finally, the system age may be estimated from the observed rotation period of the star (or, if the rotation period is not known, from the projected rotation period $P_{\rm rot}/\sin i$ determined from the spectroscopically determined $v \sin i$ and the radius determined as above) and the empirical gyrochronology relations of E. E. Mamajek & L. A. Hillenbrand (2008). The resulting fits are shown in Figure 1. The derived parameters are listed in Table 5.

## 4. System Modeling

We fit each planetary system using the `juliet` code package (N. Espinoza et al. 2019) and the `dynesty` sampler (J. S. Speagle 2020). `juliet` allows for joint fitting between photometric and radial velocity data sets. For each system, we first fit two models to the RV data, one with eccentricity fixed to 0 and another that allowed the orbit to be eccentric using the $\sqrt{e}\,\sin\omega$ and $\sqrt{e}\,\cos\omega$ parameterization. We then compared the log evidence to determine which model is supported, given the data. We used the Jeffreys scale (H. Jeffreys 1939) to interpret the resulting odds ratio for each planet. For seven systems, there was moderate evidence to support the circular orbit, with odds ratios ranging between 7.3 and 19.4. The remaining two planets, WASP-149 and WASP-195, showed weak evidence supporting the circular orbit, with odds ratios of 3.7 and 2.9, respectively. For these two planets, we jointly fit the photometry and radial velocity data with and without eccentricity. In both cases, the circular model was preferred, with an odds ratio of 252 tor WASP-149 and an odds ratio of 6239 for WASP-195. Therefore, in all cases, we held the eccentricity fixed for the final global (transit + RV) modeling.

For all models, we use the approximate Matérn kernel Gaussian process (GP) to account for the presence of stellar or systematic variability in TESS data. We used the pipeline-produced detrended lightcurves from WASP and HATNet, binned to a 5 minute cadence. For other ground-based transit observations, we fit models with and without linear detrending to airmass. When the log evidence favors the detrending, we incorporate it into the final model. Appendix B provides a full

---

[47] https://github.com/sousasag/ARES

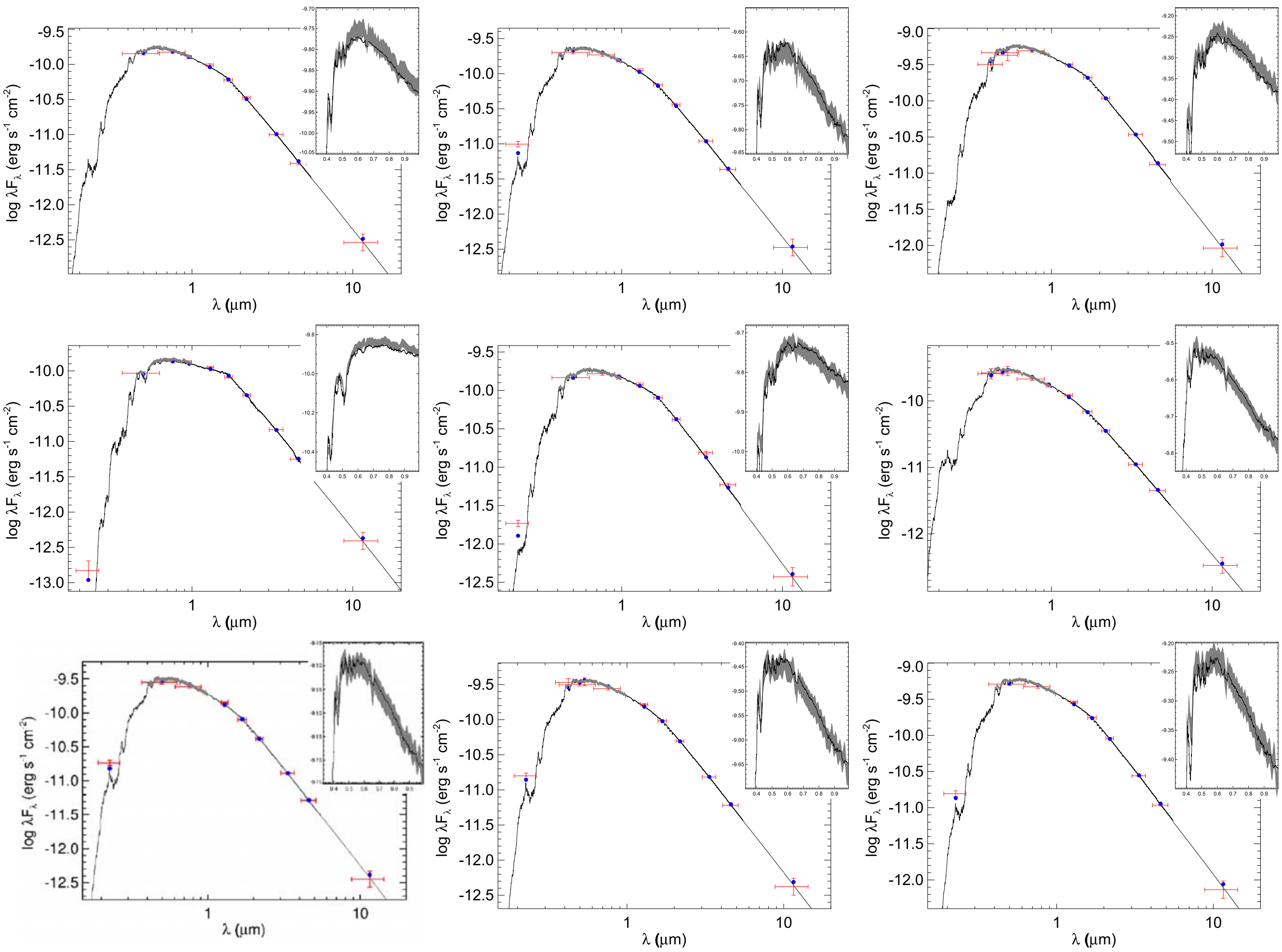

**Figure 1.** Spectral energy distributions of WASP-102 (top row, left), WASP-116 (top row, middle), WASP-149 (top row, right), WASP-154 (second row, left), WASP-155 (second row, middle), WASP-188 (second row, right), WASP-194 (bottom row, left), WASP-195 (bottom row, middle), and WASP-197 (bottom row, right). Red symbols represent the observed photometric measurements, where the horizontal bars represent the effective width of the passband. Blue symbols are the model fluxes from the best-fit PHOENIX atmosphere model (black). The absolute flux-calibrated Gaia spectrum is shown as a gray swathe in the inset figure.

list of the parameters used for each system, including any detrending parameters used.

The final fit parameters were period ($P$), epoch (t0), impact parameter ($b$), planet-to-star radius ratio ($R_p/R_*$), stellar density ($\rho_*$), and RV semi-amplitude (K). All data sets are fit with an additional baseline offset parameter, as well as a jitter term. We use the $q_1$, $q_2$ parameterization for quadratic limb darkening (D. M. Kipping 2013), with priors set from values determined using `ldtk` (T. O. Husser et al. 2013; H. Parviainen & S. Aigrain 2015). Limb-darkening parameters are shared for observations taken using the same photometric filter. For WASP and HAT, the data do not highly constrain limb darkening, so we share their parameters with that of TESS.

The TESS and TESS-SPOC pipelines account for the contribution of nearby sources in the `PDCSAP` lightcurve product, and the QLP pipeline applies deblending for additional sources within the target aperture. These contamination-correction methods rely on brightness estimates of nearby Gaia sources in the TESS input catalog, so we include the additional dilution term to account for any resulting over- or undercorrections. This term is defined in Juliet as $D = \frac{1}{1+\sum_n F_n / F_T}$, where the dilution ($D$) is a number between 0 and 1, with 1 being no additional dilution. More details on the model fits can be found in the sections below, and a summary of the results of the final fits can be found in Table 6. All data sets used in the final models are available through DRUM.[48]

### 4.0.1. WASP-102

WASP-102 b was first publicly alerted in F. Faedi et al. (2016). We present here a reanalysis of the data used in this work and updated with new TESS observations (see Figure 2). WASP-102 is a well-isolated star with low contamination in TESS and WASP data. High-contrast imaging of the star by SOAR rules out a close contaminant within 4.9 mag at a separation of 1".

After WASP identified this planet candidate, ground-based photometric observations were made by EulerCam (Gunn-$r$ filter) as well as TRAPPIST (blue-blocking filter) in 2013, obtaining a total of five full transits. Radial velocity measurements were also collected by SOPHIE and CORALIE. TESS observed the star in Sector 56 in the full-frame images at a 200 s cadence. The QLP faint-star search identified this as a planet candidate in March of 2023. The transit was also detected in the TESS-SPOC FFI lightcurve search of this sector, and the location of WASP-102 was located within 0.967 ± 2.5 of the transit source location by

---

[48] http://hdl.handle.net/1903/33819.

**Table 5**

Stellar Properties for the Planets' Host Stars

| | WASP-102 TOI-6170 | WASP-116 TOI-4672 | WASP-149 TOI-6101 | WASP-154 TOI-5288 | WASP-155 TOI-6135 |
|---|---|---|---|---|---|
| Identifiers | | | | | |
| TIC ID | 51637609 | 332911893 | 19342878 | 857186 | 100909102 |
| 2MASS | J22255144+1551242 | J02205177-0149337 | J08161768-0841121 | J21505262-0838084 | J23115512+3302519 |
| Gaia DR3 | 2736318583335936128 | 2493785078665571200 | 3062565055055954304 | 2618260274650146048 | 1910906408272899328 |
| Magnitudes | | | | | |
| TESS | 12.1 | 11.9 | 10.8 | 12.2 | 12.0 |
| $B$ | 13.4 | 13.0 | 12.3 | 14.1 | 12.9 |
| $V$ | 12.7 | 12.5 | 11.7 | 13.2 | 12.4 |
| Gaia | 12.6 | 12.3 | 11.3 | 12.8 | 12.5 |
| $J$ | 11.5 | 11.3 | 10.2 | 11.3 | 11.3 |
| $H$ | 11.2 | 11.1 | 9.9 | 10.9 | 10.9 |
| K | 11.1 | 11.0 | 9.8 | 10.8 | 10.9 |
| WISE 3.4 $\mu$m | 11.1 | 11.0 | 9.8 | 10.7 | 10.6 |
| WISE 4.6 $\mu$m | 11.1 | 11.0 | 9.8 | 10.7 | 10.7 |
| WISE 12 $\mu$m | 11.0 | 10.9 | 9.8 | 10.7 | 10.8 |
| WISE 22 $\mu$m | 9.0 | 8.6 | 8.4 | 9.1 | 9.0 |
| Properties | | | | | |
| R.A. (J2000) | 22:25:51.43 | 02:20:51.78 | 08:16:17.68 | 21:50:52.6 | 23:11:55.13 |
| Decl. (J2000) | +15:51:23.9 | −01:49:33.75 | −08:41:11.69 | −08:38:09.4 | +33:02:51.4 |
| pm (R.A.) mas yr$^{-1}$ | −13.6549 ± 0.0156 | 8.6868 ± 0.0189 | −1.5381 ± 0.0269 | −24.4276 ± 0.0188 | 18.6723 ± 0.0118 |
| pm (decl.) mas yr$^{-1}$ | −24.0709 ± 0.0145 | 1.7498 ± 0.0156 | 23.0363 ± 0.0216 | −57.1313 ± 0.0156 | −28.3813 ± 0.0109 |
| Parallax mas | 1.9564 ± 0.0150 | 1.9009 ± 0.0166 | 4.6465 ± 0.0231 | 4.4212 ± 0.0178 | 2.5810 ± 0.0115 |
| Distance pc | 535.689 ± 15.6205 | 559.243 ± 15.677 | 211.73 ± 1.688 | 215.501 ± 1.962 | 399.63 ± 4.884 |
| $T_{\rm eff}$ (K) | 5990 ± 100 | 6250 ± 125 | 5750 ± 125 | 4774 ± 133 | 5660 ± 100 |
| [Fe/H] | −0.2 ± 0.3 | 0.0 ± 0.3 | 0.0 ± 0.3 | 0.2 ± 0.1 | 0.0 ± 0.3 |
| $M_*$ ($M_\odot$) | 1.08 ± 0.07 | 1.25 ± 0.08 | 1.05 ± 0.06 | 0.80 ± 0.05 | 1.09 ± 0.07 |
| $R_*$ ($R_\odot$) | 1.375 ± 0.048 | 1.426 ± 0.064 | 1.080 ± 0.049 | 0.823 ± 0.047 | 1.240 ± 0.060 |
| log ($g$) | 4.20 ± 0.15 | 4.25 ± 0.15 | 4.40 ± 0.15 | 4.47 ± 0.08 | 4.3 ± 0.15 |
| $F_{\rm bol}$ (erg s$^{-1}$ cm$^{-2}$) | 2.686 ± 0.035 | 3.23 ± 0.11 | 7.94 ± 0.18 | 1.985 ± 0.046 | 3.03 ± 0.20 |
| Age (Gyr) | 0.67 ± 0.07 | 1.7 ± 0.8 | 0.6 ± 0.3 | | 1.7 ± 0.8 |
| RUWE[a] | 1.1096977 | 1.19287 | 1.2159479 | 1.0076779 | 0.9177554 |

| | WASP-188 TOI-5190 | WASP-194 TOI-3791 HAT-P-71 | WASP-195 TOI-4056 | WASP-197 TOI-5385 |
|---|---|---|---|---|
| Identifiers | | | | |
| TIC ID | 289574465 | 400432230 | 232567319 | 85266608 |
| 2MASS | J18350767+3636562 | J19413306+5613043 | J16301192+4953446 | J10423138+2811550 |
| Gaia DR3 | 2095929368839731072 | 2139082524468869248 | 1411707818360668416 | 734156218947945216 |
| Magnitudes | | | | |
| TESS | 11.7 | 11.6 | 11.4 | 10.9 |
| $B$ | 12.5 | 12.7 | 12.3 | 11.9 |
| $V$ | 12.2 | 12.0 | 11.9 | 11.6 |
| Gaia | 12.0 | 11.9 | 11.8 | 11.2 |
| $J$ | 11.3 | 11.1 | 10.9 | 10.3 |
| H | 11.1 | 10.9 | 10.7 | 10.1 |
| $K$ | 11.0 | 10.9 | 10.7 | 10.0 |
| WISE 3.4 $\mu$m | 11.0 | 10.8 | 10.6 | 10.0 |
| WISE 4.6 $\mu$m | 11.0 | 10.8 | 10.7 | 10.0 |
| WISE 12 $\mu$m | 10.9 | 10.8 | 10.6 | 10.0 |
| WISE 22 $\mu$m | 9.3 | 9.5 | 9.6 | 8.8 |
| Properties | | | | |
| R.A. (J2000) | 18:35:07.67 | 19:41:33.05 | 16:30:11.91 | 10:42:31.37 |
| Decl. (J2000) | +36:36:56.28 | +56:13:04.1 | +49:53:44.85 | +28:11:55.05 |
| pm (R.A.) mas yr$^{-1}$ | −0.2471 ± 0.0110 | −4.5138 ± 0.0113 | −3.8919 ± 0.0120 | −9.2100 ± 0.0190 |
| pm (decl.) mas yr$^{-1}$ | −1.3574 ± 0.0117 | −14.8880 ± 0.0125 | 14.5456 ± 0.0138 | 0.8583 ± 0.0193 |
| Parallax mas | 1.4310 ± 0.0098 | 2.0635 ± 0.0089 | 2.0266 ± 0.0102 | 2.0927 ± 0.0209 |
| Distance pc | 675.281 ± 9.674 | 476.831 ± 3.860 | 484.852 ± 5.091 | 483.675 ± 12.2885 |
| $T_{\rm eff}$ (K) | 6850 ± 125 | 6405 ± 200 | 6300 ± 125 | 6050 ± 100 |
| [Fe/H] | 0.0 ± 0.3 | 0.00 ± 0.25 | 0.0 ± 0.3 | 0.0 ± 0.3 |

**Table 5**
(Continued)

| | WASP-102<br>TOI-6170 | WASP-116<br>TOI-4672 | WASP-149<br>TOI-6101 | WASP-154<br>TOI-5288 | WASP-155<br>TOI-6135 |
|---|---|---|---|---|---|
| $M_*$ ($M_\odot$) | $1.50 \pm 0.09$ | $1.29 \pm 0.08$ | $1.30 \pm 0.08$ | $1.36 \pm 0.08$ | |
| $R_*$ ($R_\odot$) | $1.830 \pm 0.069$ | $1.409 \pm 0.090$ | $1.578 \pm 0.066$ | $2.112 \pm 0.077$ | |
| log ($g$) | $4.10 \pm 0.2$ | $4.27 \pm 0.5$ | $4.14 \pm 0.25$ | $3.9 \pm 0.2$ | |
| $F_{\rm bol}$ (erg s$^{-1}$cm$^{-2}$) | $4.355 \pm 0.050$ | $4.101 \pm 0.096$ | $4.65 \pm 0.11$ | $7.55 \pm 0.18$ | |
| Age (Gyr) | | $0.75 \pm 0.55$ | $0.6 \pm 0.2$ | $2.6 \pm 1.5^{*}$ | |
| RUWE[a] | 0.8776204 | 0.95639163 | 0.8457882 | 0.99257046 | |

**Notes.** Details on spectral line fitting and SED modeling can be found in Section 3.
[a] Gaia renormalized unit weight error (RUWE). Values ≈1 are expected for single sources, while values $\gtrsim$1.4 suggest extended or binary sources.

the difference image centroiding analysis in the TESS-SPOC Data Validation (DV) report (J. D. Twicken et al. 2018).

We jointly fit the WASP, TESS, TRAPPIST, EulerCam, SOPHIE, and CORALIE data. We include GP detrending for TESS and linear detrending model with airmass for the ground-based follow-up observations. Consistent with F. Faedi et al. (2016), who reported $M_{\rm pl} = 0.62 \pm 0.05\ M_{\rm Jup}$ and $R_{\rm pl} = 1.26 \pm 0.02\ R_{\rm Jup}$, we find the planet to have a mass of $0.62 \pm 0.13\ M_{\rm Jup}$ and a radius of $1.33 \pm 0.05\ R_{\rm Jup}$.

### 4.0.2. *WASP-116*

WASP-116 was observed by both SuperWASP and WASP-South from 2008 August through 2010 December. A planet transit was identified in this combined data set, leading to spectroscopic follow-up by both the SOPHIE and CORALIE instruments. Additional photometric follow-up was taken by TRAPPIST and EulerCam, with the two instruments simultaneously observing two different transit ingress events. WASP-116 b was subsequently publicly announced by D. J. A. Brown et al. (2014).

TESS observed this target in the 30 minute cadence FFIs in the primary mission. The target was revisited by TESS in its first mission extension, in which the FFI cadence was reduced to 10 minutes. The QLP Faint Star Search (M. Kunimoto et al. 2022) identified this target as a TOI in 2021 December, following these observations. After being given a TOI designation, several observations were submitted through TFOP, including LCOGT observations from SAAO and Haleakala taken with the *i'* filter. We note that an additional observation was submitted from Hazelwood observatory using a Sloan *g'* filter. However, an ill-timed gap due to clouds immediately following the meridian flip coinciding with the transit egress make the transit depth difficult to constrain. We therefore remove this data set from our analysis. The final best-fit transit and RV models can be seen in Figure 3. We find the planet is in a 6.61 day orbit, with a mass of $0.64 \pm 0.14\ M_{\rm Jup}$ and a radius of $1.22 \pm 0.06\ R_{\rm Jup}$, which are consistent with the values of $0.59 \pm 0.05\ M_{\rm Jup}$ and $1.43 \pm 0.07\ R_{\rm Jup}$ found in D. J. A. Brown et al. (2014) within $2\sigma$.

### 4.0.3. *WASP-149*

Like WASP-116 b, WASP-149 b was introduced in D. J. A. Brown et al. (2014). The star was observed by both SuperWASP and WASP South from 2009 November through 2012 March. A joint analysis of the WASP data sets identified a planetary candidate, leading to SOPHIE and CORALIE radial velocity measurements. Photometric follow-up from NITES, TRAPPIST, and EulerCam were also collected; however, NITES data from the initial analysis were not recovered and could not be included in this analysis.

WASP-149 was later observed by TESS FFIs with a 30 minute cadence in Sector 7 and 10 minute cadence in Sector 34. When it was again reobserved in Sector 61, the star was selected for a 2 minute cutout data, and it was processed by the SPOC pipeline. The transit was identified by SPOC, with centroiding analysis locating the transit source to $0.''47 \pm 2.''4$.

For TESS, we include only the 2 minute data in our final analysis. As part of the TFOP program, MuSCAT2 observations containing an egress event were uploaded to the ExoFOP webpage. The multiband observations are consistent in depth, supporting the planet interpretation. However, the lack of a pre-transit baseline makes a definitive depth analysis impossible, and we do not include the data in the global analysis. However, deep eclipses from nearby targets can be ruled out from this data set.

The final planet model along with the data used can be seen in Figure 4. Orbiting with a period of 1.33 days, WASP-149 b has the shortest period of the planets presented in this work. The mass of $0.99 \pm 0.20\ M_{\rm Jup}$ and a radius of $1.36 \pm 0.06\ R_{\rm Jup}$ are consistent within $1\sigma$ to the values of $1.02 \pm 0.04\ M_{\rm Jup}$ and $1.32 \pm 0.04\ R_{\rm Jup}$ found in D. J. A. Brown et al. (2014).

### 4.0.4. *WASP-154*

WASP-154 was observed by both SuperWASP and WASP South facilities from 2008 June to 2010 October. After being identified as a planet candidate in 2013, radial velocity follow-up from SOPHIE began. In addition, observations of the full transit were captured by TRAPPIST, EulerCam, and NITES.

This target was subsequently observed in TESS Sector 42 FFIs with a 10 minute cadence. The TESS-SPOC identified the transit, with centroiding analysis showing the transit location within $0.''82 \pm 2.''50$ from the star. The QLP faint target search (M. Kunimoto et al. 2022) identified this as a TOI in 2022. This triggered additional photometric follow-up observations at the LCO/CTIO and Brierfield facilities. The final transit and RV models along with the data used in the model are found in Figure 5. The results show this is a nearly Jupiter-sized planet ($R_{\rm pl} = 0.96 \pm 0.06\ R_{\rm Jup}$) but with a mass of $0.63 \pm 0.13\ M_{\rm Jup}$ in a 3.81 day orbit.

### 4.0.5. *WASP-155*

WASP-155 was observed by SuperWASP from 2004 May through 2007 November. In 2014, the WASP team identified the lightcurve as a potential planet transit and initiated SOPHIE radial velocity measurements. Initial observations showed the RVs were in phase and suggested a planetary mass, and a

**Table 6**
Summary of Fit and Derived Planetary System Parameters for the Nine Giant Planets

| | WASP-102<br>TOI-6170 | WASP-116<br>TOI-4672 | WASP-149<br>TOI-6101 | WASP-154<br>TOI-5288 | WASP-155<br>TOI-6135 |
|---|---|---|---|---|---|
| Fit Parameters | | | | | |
| $P$ (days) | 2.709813 ± 3e-7 | 6.61320 ± 2e-06 | $1.332813\ ^{6e-7}_{5e-7}$ | 3.811678 ± 1e-06 | 3.110413 ± 1e-06 |
| t0 (BJD-2450000) | $7109.45577\ ^{+1.6e-4}_{-1.7e-4}$ | $7092.22528\ ^{+5.3e-4}_{-4.9e-4}$ | 7757.62450 ± 8e-5 | $9465.89195\ ^{+2.8e-4}_{-2.7e-4}$ | 9852.08494 ± 4.1e-4 |
| $b$ | $0.11\ ^{+0.06}_{-0.04}$ | $0.07\ ^{+0.06}_{-0.05}$ | 0.58 ± 0.005 | 0.31 ± 0.04 | 0.43 ± 0.02 |
| $R_{\rm pl}/R_*$ | 0.0997 ± 0.0004 | 0.0881 ± 0.0004 | $0.1297\ ^{+0.0008}_{-0.0009}$ | 0.12 ± 0.001 | $0.0997\ ^{+0.0015}_{-0.0014}$ |
| $\rho_*$ (g cm$^{-3}$) | $0.684\ ^{+0.011}_{-0.016}$ | $0.404\ ^{+0.007}_{-0.010}$ | 1.180 ± 0.009 | $2.012\ ^{+0.067}_{-0.066}$ | $0.803\ ^{+0.014}_{-0.011}$ |
| $K$ (m s$^{-1}$) | $86.16\ ^{+4.37}_{-4.28}$ | $59.67\ ^{+3.09}_{-3.01}$ | $175.25\ ^{+5.19}_{-5.31}$ | $94.55\ ^{+2.46}_{-2.44}$ | $114.29\ ^{+2.50}_{-2.53}$ |
| eccentricity | 0 (fixed) | 0 (fixed) | 0 (fixed) | 0 (fixed) | 0 (fixed) |
| Derived Parameters | | | | | |
| Rp ($R_{\rm Jup}$) | 1.33 ± 0.05 | 1.22 ± 0.06 | 1.36 ± 0.06 | 0.96 ± 0.06 | 1.20 ± 0.06 |
| Mp ($M_{\rm Jup}$) | 0.622 ± 0.133 | 0.64 ± 0.14 | 0.991 ± 0.196 | 0.626 ± 0.129 | 0.871 ± 0.18 |
| pl density (g cm$^{-3}$) | 0.32 ± 0.08 | 0.43 ± 0.12 | 0.49 ± 0.12 | 0.88 ± 0.25 | 0.62 ± 0.17 |
| depth (ppm) | 9949 ± 986 | 7763 ± 989 | 16834 ± 2170 | 14400 ± 2338 | $9940\ ^{1393}_{-1388}$ |
| $a/R_s$ | $6.43\ ^{+0.04}_{-0.05}$ | $9.77\ ^{+0.05}_{-0.08}$ | 4.8 ± 0.01 | 11.56 ± 0.13 | 7.43 ± 0.04 |
| $a$ (au) | 0.041 ± 0.001 | 0.065 ± 0.003 | 0.024 ± 0.001 | 0.044 ± 0.003 | 0.043 ± 0.002 |
| $i$ (deg) | $89.06\ ^{+0.57}_{-0.39}$ | $89.57\ ^{+0.05}_{-0.28}$ | $83.02\ ^{+0.38}_{-0.37}$ | $88.46\ ^{+0.3}_{-0.27}$ | 86.7 ± 0.29 |
| $T_{\rm eq}$ (K) | 1671 ± 65 | 1414 ± 70 | 1855 ± 93 | 994 ± 63 | 1468 ± 76 |
| $S_{\rm pl}$ ($S_\oplus$) | 1293 ± 155 | 663 ± 100 | 1966 ± 305 | 162 ± 31 | 771 ± 119 |
| TSM[a] | 86 ± 20 | 54 ± 13 | 189 ± 43 | 57 ± 14 | 54 ± 13 |
| | WASP-188<br>TOI-5190 | WASP-194<br>TOI-3791<br>HAT-P-71 | WASP-195<br>TOI-4056 | WASP-197<br>TOI-5385 | |
| Fit Parameters | | | | | |
| $P$ (days) | 5.748916 ± 3e-06 | $3.183387\ ^{4e-7}_{5e-7}$ | 5.051928 ± 4e-6 | 5.167228 ± 3e-06 | |
| t0 (BJD-2450000) | 7033.12141 ± 0.001 | 7449.0511 ± 0.0003 | $7357.23855\ ^{+0.0022}_{-0.00185}$ | $6885.10428\ ^{+0.00166}_{-0.00173}$ | |
| $b$ | 0.61 ± 0.01 | 0.84 ± 0.040 | 0.55 ± 0.01 | 0.43 ± 0.02 | |
| $R_{\rm pl}/R_*$ | 0.0742 ± 0.0005 | 0.1007 ± 0.0004 | $0.0600\ ^{+0.0018}_{-0.0016}$ | 0.0627 ± 0.0007 | |
| $\rho_*$ (g cm$^{-3}$) | 0.345 ± 0.002 | $0.683\ ^{+0.027}_{-0.016}$ | $0.466\ ^{+0.004}_{-0.003}$ | 0.204 ± 0.002 | |
| $K$ (m s$^{-1}$) | $124.63\ ^{+5.82}_{-6.49}$ | $135.90\ ^{+13.42}_{-13.26}$ | $10.32\ ^{+2.16}_{-2.19}$ | $121.32\ ^{+3.7}_{-3.59}$ | |
| eccentricity | 0 (fixed) | 0 (fixed) | 0 (fixed) | 0 (fixed) | |
| Derived Parameters | | | | | |
| Rp ($R_{\rm Jup}$) | 1.322 ± 0.051 | 1.381 ± 0.088 | 0.92 ± 0.05 | 1.289 ± 0.049 | |
| Mp ($M_{\rm Jup}$) | $1.443\ ^{+0.296}_{-0.298}$ | 1.174 ±0.265 | $0.104\ ^{0.03}_{0.031}$ | 1.269 ± 0.254 | |
| pl density (g cm$^{-3}$) | 0.78 ± 0.20 | 0.55 ± 0.18 | 0.16 ± 0.06 | 0.74 ± 0.18 | |
| depth (ppm) | 5509 ± 593 | 10143 ± 1835 | $3602\ ^{+477}_{-466}$ | $3931\ ^{+414}_{-415}$ | |
| $a/R_s$ | 8.46 ± 0.01 | 7.15 ± 0.09 | 8.57 ± 0.02 | 6.6 ± 0.03 | |
| $a$ (au) | 0.072 ± 0.003 | 0.047 ± 0.003 | 0.063 ± 0.003 | 0.065 ± 0.002 | |
| $i$ (deg) | 85.88 ± 0.20 | $83.23\ ^{+0.47}_{-0.46}$ | 86.30 ±0.25 | 86.29 ± 0.32 | |
| $T_{\rm eq}$ (K) | 1666 ± 70 | 1693 ± 122 | 1522 ± 71 | 1665 ± 67 | |
| $S_{\rm pl}$ ($S_\oplus$) | 1278 ± 165 | 1365 ± 303 | 890 ± 127 | 1276 ± 157 | |
| TSM[a] | 23 ± 5 | 59 ± 16 | 153 ± 48 | 28 ± 6 | |

**Notes.** A full list of fitted parameters and prior values can be found in Appendix B, and corner plots for key system parameters are presented in Appendix A.

[a] Transmission spectroscopy metric (E. M. R. Kempton et al. 2018).

photometric follow-up observation by NITES further confirmed the transit.

The star was included in the FFI images from TESS Sector 56 at a 200 s cadence and identified as a TOI in the faint-star search using the QLP pipeline (M. Kunimoto et al. 2022). We use the detrended and deblended data (`det_flux`) from the QLP pipeline in our fit. The MuSCAT2 instrument made four multiband observations of WASP-155 and found achromatic transits across the $g$, $r$, $i$, and $z_s$ bands. In our final fit, we include only one of these full-transit multiwavelength observations (See Figure 6).

Speckle images taken as part of the TFOP tentatively suggests a faint companion ~3" from the target with a Δmag of 5.26 using the 832 nm filter. Gaia also reports a companion at the same separation, with a Δmag of 2.55 in the Gaia passband. Due to the wide separation, the Δmag value measured in the speckle data is likely to be overestimated. There are two effects to consider, both of which would lead to an anomalously large Δmag. One is that the companion star fell close to the edge of the CCD readout region, causing some of the companion star's speckle patterns to lie outside of this region and go undetected. Additionally, the correlation of adjacent speckle patterns decreases with increasing angular separation, and this has not been accounted for in the NESSI photometry. The reported Gaia parallax and proper motion for both stars are similar,

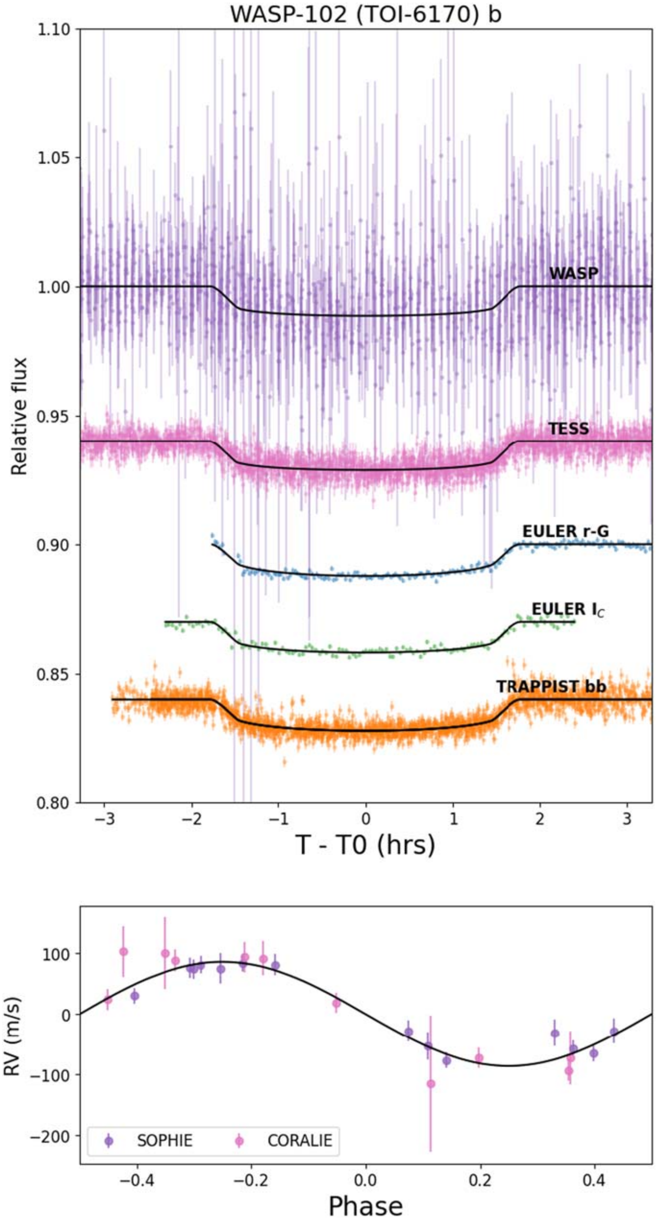

**Figure 2.** Transit and RV fit for WASP-102 b. Transit observations are offset for clarity. The three TRAPPIST observations were taken with the same filter, and they are plotted together.

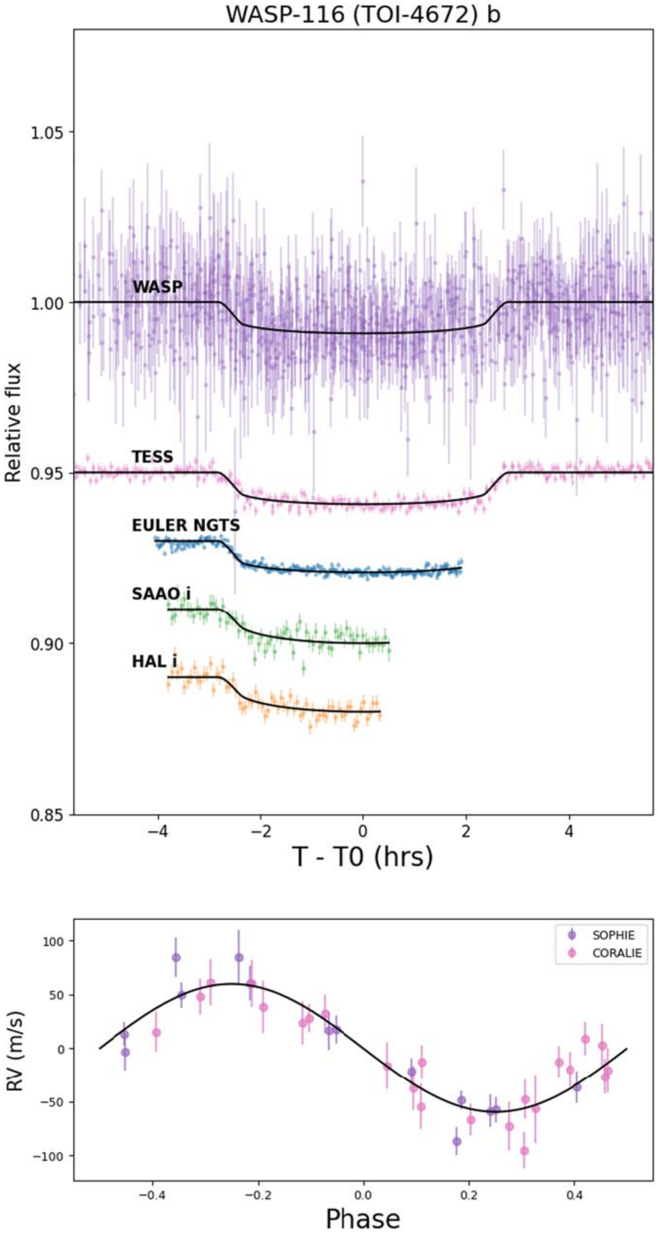

**Figure 3.** Global fit for WASP 116 b. Photometric lightcurves have been offset for visual clarity.

suggesting that the stars may be bound. More observations could determine whether this is truly a binary pair. The proximity to the nearby star leads to blending within the target aperture in the photometric observations. We therefore center the prior for the dilution factor to the expected dilution resulting from a source with Δmag 2.55 as seen by Gaia.

We find WASP-155 b to be a 1.91 $R_{\mathrm{Jup}}$, 0.86 $M_{\mathrm{Jup}}$ planet orbiting with a period of 3.11 days. The estimated temperature of the planet is just shy of 1500 K.

#### *4.0.6. WASP-188*

WASP-188 was observed by SuperWASP from 2004 May through 2010 August and flagged as a planet candidate in 2014. RV observations with SOPHIE showed variations in phase with the transit period. Subsequent multiband photometric observations by MuSCAT2 and KeplerCam were made to refine the ephemeris as well as check for achromatic depths. The observations for KeplerCam and MuSCAT2 were binned to a 2 minute cadence to reduce scatter during the model fit.

Gaia observations revealed that WASP-188 has a close companion (Δmag ≈5.5) at $1\overset{''}{.}81$, which was confirmed by speckle images taken at SAI, contributing flux to the photometric apertures. The TESS-SPOC PDCSAP lightcurve does take into account the contamination of this and other nearby stars in the aperture using the CROWDSAP (crowding) and FLFRCSAP (completeness) measures. However, there is still blending in the MuSCAT2 and KeplerCam lightcurves even with the smaller pixel scales. We set the dilution prior for these data sets based on the expected dilution for a target with the reported magnitude difference. The resulting fit can be found in Figure 7. We find the planet to have a radius of $1.33 \pm 0.05$ $R_{\mathrm{Jup}}$ and a mass of $1.52^{+0.32}_{-0.31}$ $M_{\mathrm{Jup}}$.

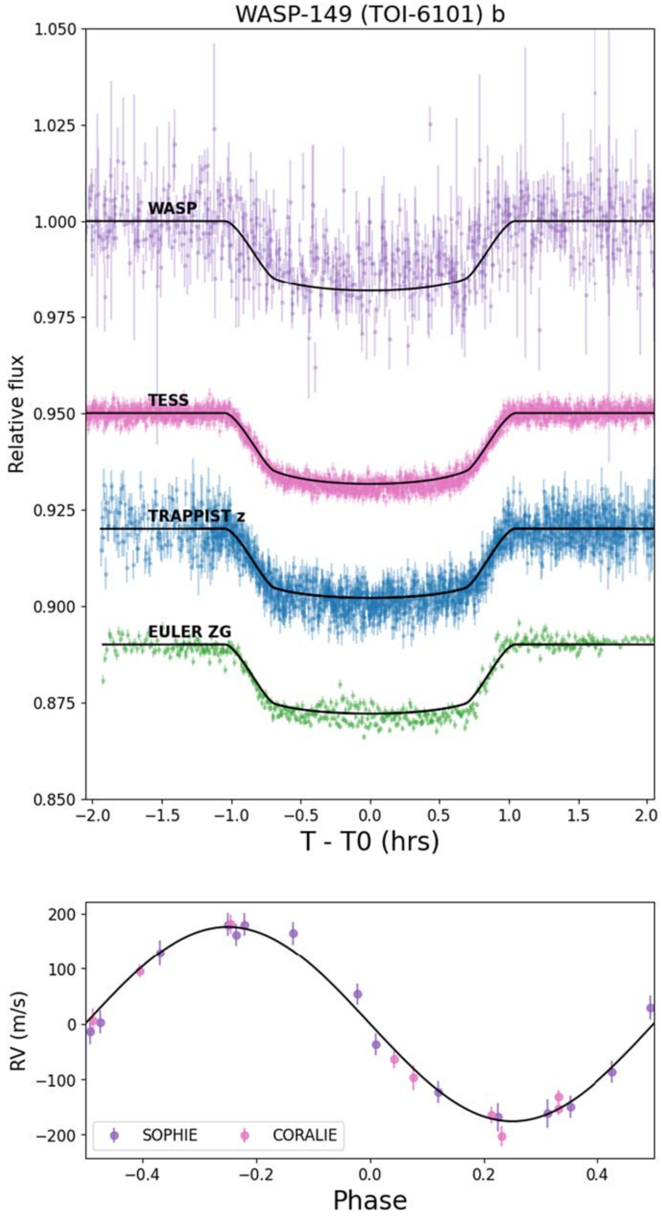

**Figure 4.** Final joint transit and RV model fit for WASP-149 b. The top panels show the available photometric data, offset for clarity. The bottom panel shows the final RV fit for SOPHIE and CORALIE data.

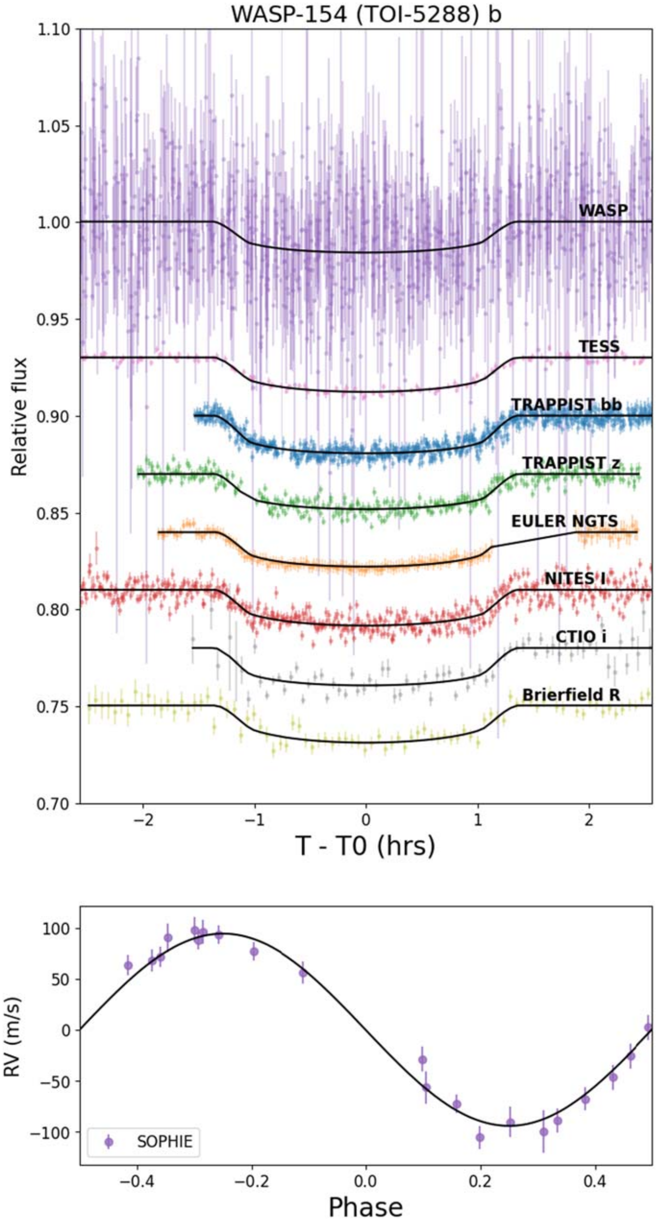

**Figure 5.** Final joint transit and RV model fit for WASP-154 b. The top panel shows the photometric data sets, offset for clarity, while the bottom panel shows the fit to the radial velocity data.

### *4.0.7. WASP-194/HAT-P-71*

WASP-194 b was independently identified as a planet candidate with a 3.32 day period by both the WASP and HATNet (G. Bakos et al. 2004) surveys. TRES radial velocity observations of this target began in 2013, showing that the object was consistent with a planetary mass. KeplerCam confirmed and refined the transit with eight observations spanning from 2014 to 2017. TESS observed this target in FFIs in Sectors 14, 15, 16, and 20. The star was elevated to a TOI through the QLP faint-star search. Subsequent TESS Sectors observed this star with 2 minute cutouts. Additional ground-based follow-up observations were taken by MuSCAT2 and RC 8GSO.

The final fit for this planet (see Figure 8) included photometric data from WASP and HAT, 120 s lightcurves produced by the SPOC for TESS Sectors 40, 41, 50, 54, 55, 56, 57, and 60, MuSCAT2 observations in $g$, $r$, $i$, $z_{\rm z}$, and one full KeplerCam and OPM observation, as well as the TRES RV data. The planet is found to have a mass of $1.17 \pm 0.27\ M_{\rm Jup}$ and a radius of $1.38 \pm 0.09\ R_{\rm Jup}$.

### *4.0.8. WASP-195*

WASP-195 b was first flagged as a planet candidate with a 5.05 day orbit by WASP in 2014 February. Shortly after, extensive RV follow-up observations by SOPHIE began, with 88 observations to date. TESS later observed the star in Sectors 23–25 in the FFIs with a cadence of 30 minutes. The star was again observed by TESS two years later in Sectors 50 and 52, this time with 2 minute cutout data, and the transit was identified as a TOI. Centroiding analysis shows the transit source is within $0\farcs076 \pm 2\farcs5$ from the star. As part of the TFOP effort, three high-resolution images were taken to identify nearby stars. These observations were able to rule out a companion within 6.5 mag at $0\farcs5$. Finally, a photometric

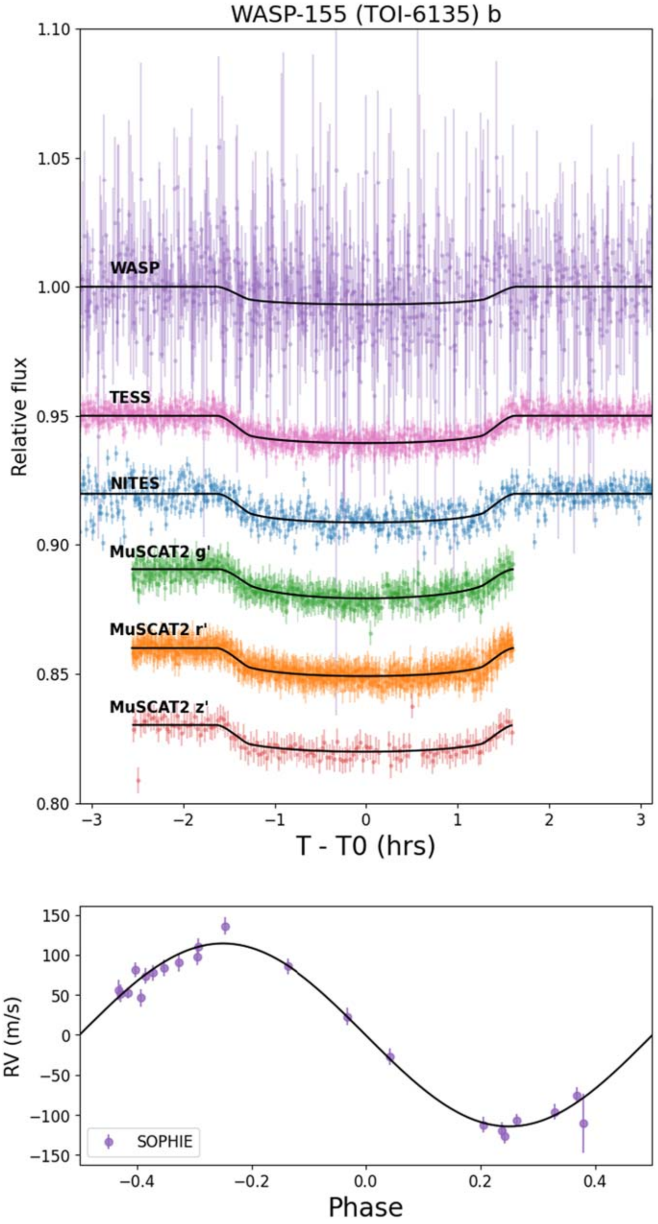

**Figure 6.** Final joint transit and RV model fit for WASP-155 b. Photometric observations are offset for clarity.

lightcurve with a Sloan *r'* filter was taken by Whitin Observatory. While conditions were cloudy, leading to a temporary stop in observations during the transit, the egress was clearly observed. We fit a transit model using WASP, TESS Sectors 50 and 52, and Whitin photometry along with SOPHIE RV measurements (Figure 9). The fit reveals a puffy planet with radius of $0.92 \pm 0.05$ $R_{\rm Jup}$ but a mass of only $0.10 \pm\ 0.03$ $M_{\rm Jup}$. We discuss this curious system in more detail in Section 5.

### 4.0.9. WASP-197

WASP-197 b was identified as a planet candidate by N. Schanche et al. (2019b), and was soon after identified as a TOI by SPOC following TESS observations in Sector 48. There is a nearby star (DR3 734156214654777984) identified by Gaia with a separation of $6\farcs7$. This star has an estimated $\Delta$mag 5.6 in the TESS bandpass. To check for possible additional nearby companions, several high-contrast imaging facilities observed the star, establishing a limit of $\Delta$6.8 mag at $0\farcs5$ in the *K* band. Combined centroiding analysis of TESS data disfavors this as a transit source, with an offset of $0\farcs362 \pm 2\farcs6$.

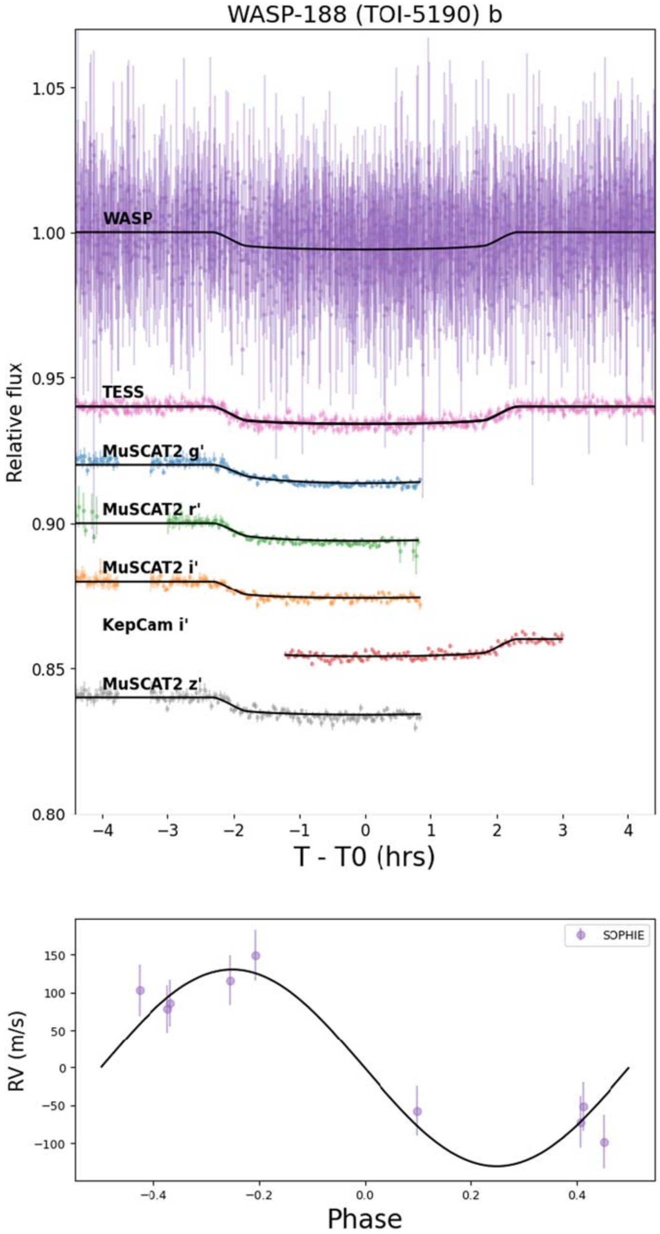

**Figure 7.** Global fit for WASP 188 b. Photometric lightcurves have been offset, and the TESS-SPOC lightcurves for Sectors 40, 53, and 54 are combined in the final plot for visual clarity. The KeplerCam and MuSCAT2 data shown here are binned to a 2 minute cadence, which was used when fitting the model.

Follow-up undertaken by three facilities, SOPHIE, TRES, and PARAS-2, showed radial velocity measurements in phase with the transit, allowing us to measure the mass of $1.27 \pm 0.25$ $M_{\rm Jup}$, establishing the transiting object as a planet (Figure 10).

## 5. Discussion

The nine giant planets presented here encompass a range of properties exhibited by the hot Jupiter population at large. All planets have periods under seven days and radii near that of Jupiter. Figures 11 and 12 show these planets in the context of the known population contained in the NASA Exoplanet Archive (accessed 2024 October 7).

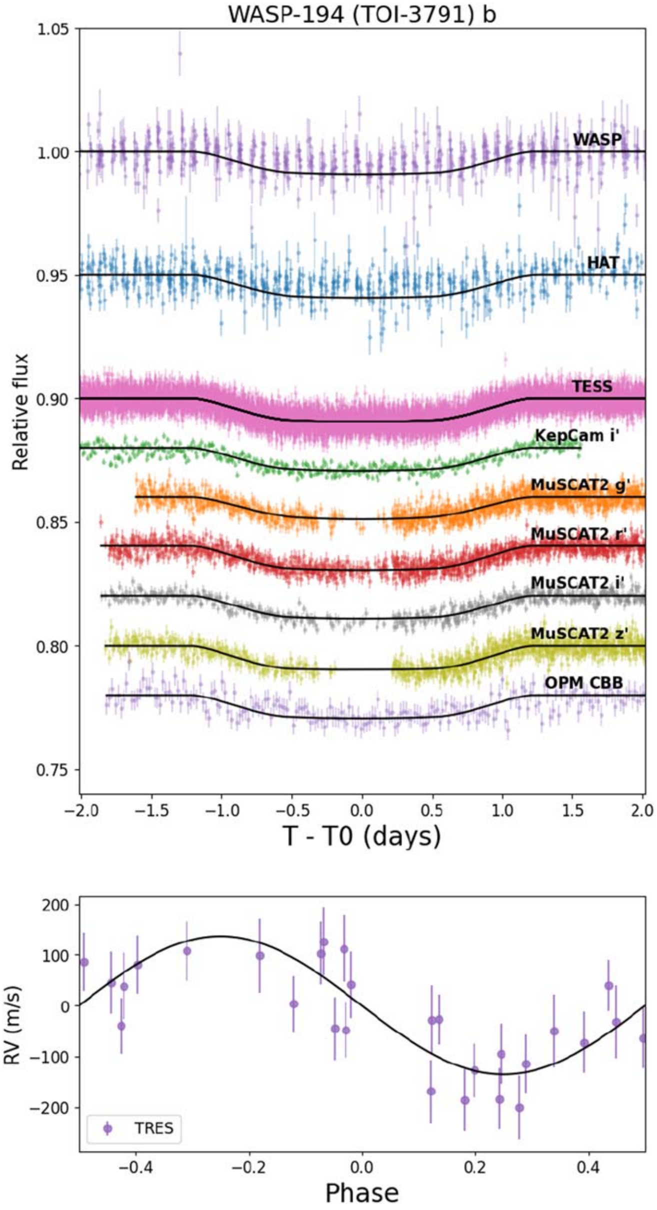

**Figure 8.** Final joint transit model fit for WASP-194 b. Photometric observations have been offset, and the eight TESS sectors of observations are combined for clarity.

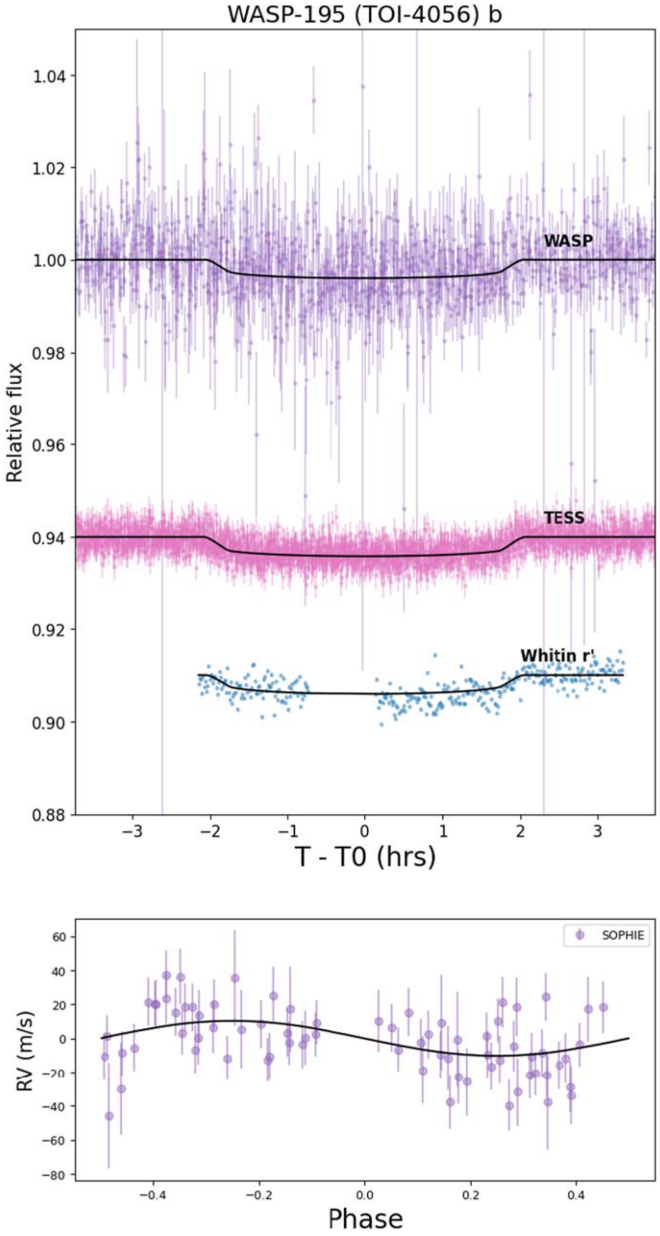

**Figure 9.** Final joint transit model fit for WASP-195 b. TESS Sectors 50 and 52 are shown together, and all lightcurves are offset for clarity.

In particular, Figure 11 shows that the planets are consistent with known hot Jupiters in terms of their radii and periods. Figure 12 demonstrates the planets reported here are generally consistent with the long-noted trend that hotter, more irradiated planets tend to have larger radii and therefore lower densities (B.-O. Demory & S. Seager 2011).

Figure 12 also illustrates that the reported planets show typical mass/radius relationships, with the exception of one planet. This outlier is WASP-195 b, which, with a radius of 0.91 $R_{\mathrm{Jup}}$ but a mass of only 0.11 $M_{\mathrm{Jup}}$, has one of the lowest densities among the currently known exoplanets.

Several low-density planets including KELT-11 b WASP-193 b, and WASP-127 b show low densities similar to that of WASP-195 b. However, these host stars are either approaching the end of their main-sequence lifetimes or are already evolving onto the red giant phase. The inflated radii in these systems are at least partially attributed to reinflation, which occurs as the levels of irradiation reaching the planets increases during the giant branch evolution stage.

The stellar models indicate that WASP-195 is a young star ($0.6 \pm 0.2$ Gyr). This means that the planet may still be cooling and contracting after the planet's formation. The expected timescale for this contraction is on the order of 1 Gyr (J. E. Owen & Y. Wu 2016). Observations of systems of various ages have supported the connection between age and inflation, with a noted trend that puffier low-mass but Jupiter-radius planets tend to be found around younger stars, whereas denser planets are found around older stars (A. Karalis et al. 2025). J. E. Libby-Roberts et al. (2020) modeled two similarly puffy sub-Neptune planets orbiting the young (≈0.5 Gyr) star Kepler-51, and found that the planets are likely undergoing contraction and mass loss, with predicted final densities approaching densities more in line with the sub-Neptune

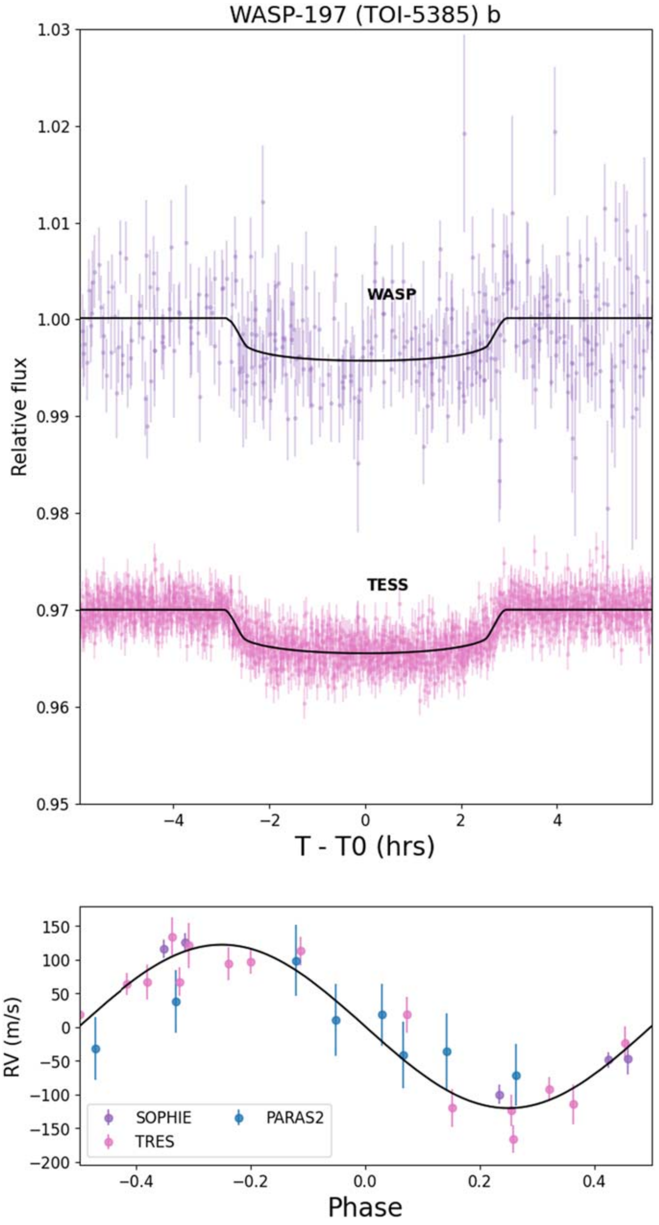

**Figure 10.** Final joint transit model fit for WASP-197 b. WASP and TESS lightcurves are offset for clarity.

population at large. Further modeling of WASP-195 b's atmospheric evolution may provide evidence for a similar fate.

In addition to contraction, migration may play a role in puffing up the atmosphere. It is proposed that the Jovian planets likely formed beyond the ice line, where fast cooling of the envelope could allow even low-mass cores to accrete a large H/He atmosphere (E. J. Lee & E. Chiang 2016). As the planets migrate inward, they are exposed to increased stellar radiation, further inflating the atmosphere (M. Mol Lous & Y. Miguel 2020).

Detailed spectral observations of WASP-195 b, combined with interior modeling, will help to determine constraints on the core and atmospheric mass ratio, providing insight into the possible formation scenarios for the planet. If indeed the planet has a substantial H/He envelope, the atmosphere may be expected to be undergoing significant mass loss that could be measured. Observations of helium lines surrounding the transit of the similarly low-density ($0.13\ \mathrm{g\ cm}^3$) WASP-107 b showed a significant absorption following the end of the transit, suggesting the atmosphere is actively being lost with a comet-like tail (J. J. Spake et al. 2021).

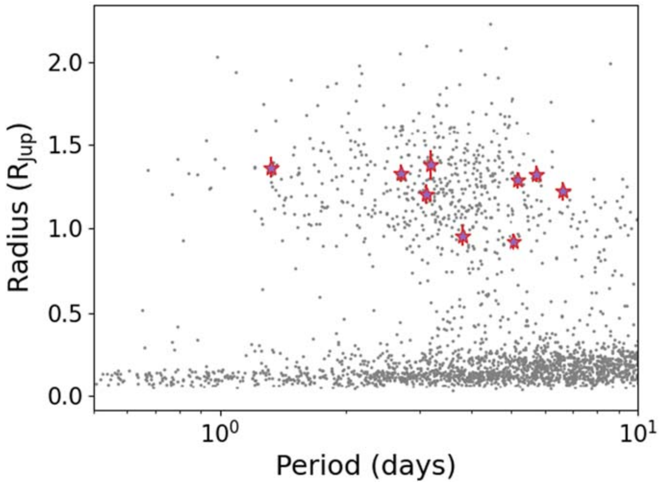

**Figure 11.** Planet period and radius. Gray points show the known planet population, while red stars show the nine new planets presented here.

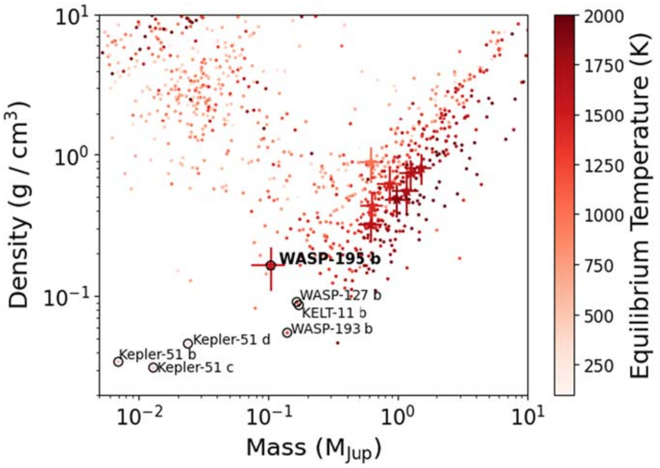

**Figure 12.** Planet mass and density. The color of the points represent the planets' equilibrium temperatures, with darker colors representing higher temperatures. Small points indicate the known population, with errorbars omitted for visual clarity. The large stars show the nine planets from this work. The "puffy" exoplanets discussed in Section 5 are circled for reference.

The eccentricity of the hot Jupiter population has important implications on the dominant formation mechanism (e.g., R. I. Dawson et al. 2015). While hot Jupiters with periods less than 3 days show mostly circular orbits, moderate eccentricities are observed in some giant planets in orbits between 3 and 10 days (see R. I. Dawson & J. A. Johnson 2018 for a review). We do not find strong support for eccentricity for any of the planets we fit here, and therefore we fix all eccentricities to 0 in our model. However, it is possible that additional RV monitoring could provide more refined measurements on the eccentricities.

## 6. Conclusion

This paper presents the characterization of nine planets (WASP-102 b, WASP-116 b, WASP-149 b, WASP-154 b, WASP-155 b, WASP-188 b, WASP-194 b/HAT-P-71 b, WASP-195 b, and WASP-197 b) orbiting FGK stars with periods under seven days. The planets were identified as candidates by transits observed by WASP and later characterized with ground-based radial velocity measurements. The planet parameters were determined by jointly fitting photometric and radial velocity measurements from a variety of sources, including TESS photometry. In addition, high-resolution imaging data were obtained for all stars, to identify and account for any previously unresolved nearby companions.

All of the host stars are relatively bright, with Gaia magnitudes less than 12.8, allowing for a variety of ground-based follow-up and characterization. The new planets provide additional samples to test our understanding of the demographics of the hot Jupiter population. While the majority of the reported planets show characteristics typical of the currently known hot Jupiter population, the masses determined from the radial velocity measurements reveal the noticeably low density of WASP-195 b. This suggests that this planet may be better characterized as a young, puffy member of the sub-Neptune population that is still undergoing contraction and mass loss. Insights into the atmospheric properties gleaned from observations with facilities such as JWST could provide the context to understand the observed low density. Further, both this planet and WASP-149 b have high transmission spectroscopy metric values (153 ± 48 and 189 ± 43), making them promising candidates for such atmospheric follow-up.

## Acknowledgments

The material is based upon work supported by NASA under award number 80GSFC24M0006.

H.P. acknowledges support by the Spanish Ministry of Science and Innovation with the Ramon y Cajal fellowship number RYC2021-031798-I. Funding from the University of La Laguna and the Spanish Ministry of Universities is acknowledged. K.K.M. acknowledges support from the New York Community Trust Fund for Astrophysical Research. The postdoctoral fellowship of K.B. is funded by F.R.S.-FNRS grant T.0109.20 and by the Francqui Foundation. M.L. acknowledges support of the Swiss National Science Foundation under grant No. PCEFP2_194576. The contribution of M.L. has been carried out within the framework of the NCCR PlanetS supported by the Swiss National Science Foundation under grant 51NF40_205606. K.A.C. acknowledges support from the TESS mission via subaward s3449 from MIT. D. R.C. acknowledges partial support from NASA Grant 18-2XRP18_2-0007. I.A.S. and P.A.B. acknowledge the support of M.V. Lomonosov Moscow State University Program of Development. S.G.S acknowledges the support from FCT through Investigador FCT contract nr. CEECIND/00826/2018 and POPH/FSE (EC). G.B. acknowledges the support from NASA grant 80NSSC22K0315.

Funding for the TESS mission is provided by NASA's Science Mission Directorate. We acknowledge the use of public TESS data from pipelines at the TESS Science Office and at the TESS-SPOC. This research has made use of the the NASA Exoplanet Archive and the Exoplanet Follow-up Observation Program (ExoFOP; 10.26134/ExoFOP5) website, which are operated by the California Institute of Technology, under contract with the National Aeronautics and Space Administration under the Exoplanet Exploration Program. Resources supporting this work were provided by the NASA High-End Computing (HEC) Program through the NASA Advanced Supercomputing (NAS) Division at Ames Research Center for the production of the SPOC data products. This paper includes data collected by the TESS mission that are publicly available from the Mikulski Archive for Space Telescopes (MAST).

Some of the observations in this paper made use of the High-Resolution Imaging instrument Zorro and were obtained under Gemini LLP Proposal Number: GN/S-2021A-LP-105. Zorro was funded by the NASA Exoplanet Exploration Program and built at the NASA Ames Research Center by Steve B. Howell, Nic Scott, Elliott P. Horch, and Emmett Quigley. Zorro was mounted on the Gemini-South telescope of the international Gemini Observatory, a program of NSF's OIR Lab, which is managed by the Association of Universities for Research in Astronomy (AURA) under a cooperative agreement with the National Science Foundation. On behalf of the Gemini partnership: the National Science Foundation (United States), National Research Council (Canada), Agencia Nacional de Investigación y Desarrollo (Chile), Ministerio de Ciencia, Tecnología e Innovación (Argentina), Ministério da Ciência, Tecnologia, Inovações e Comunicações (Brazil), and Korea Astronomy and Space Science Institute (Republic of Korea).

Some of the observations in this paper made use of the NN-EXPLORE Exoplanet and Stellar Speckle Imager (NESSI). NESSI was funded by the NASA Exoplanet Exploration Program and the NASA Ames Research Center. NESSI was built at the Ames Research Center by Steve B. Howell, Nic Scott, Elliott P. Horch, and Emmett Quigley.

We are grateful to PRL-DOS (Department of Space, Government of India), as well as the Director, PRL, for their generous support. Their support has been instrumental in funding the PARAS-2 spectrograph for our exoplanet discovery project. We express our gratitude to all the Mount Abu Observatory staff and PARAS-2 instrument team for their invaluable assistance throughout the observations.

This work makes use of observations from the LCOGT network. Part of the LCOGT telescope time was granted by NOIRLab through the Mid-Scale Innovations Program (MSIP). MSIP is funded by NSF. This paper is based on observations made with Las Cumbres Observatory's education network telescopes that were upgraded through generous support from the Gordon and Betty Moore Foundation.

Based on observations obtained at the Hale Telescope, Palomar Observatory, as part of a collaborative agreement between the Caltech Optical Observatories and the Jet Propulsion Laboratory [operated by Caltech for NASA].

We thank the Observatoire de Haute-Provence (CNRS) staff for its support. This work was supported by CNES and the "Programme National de Planétologie" (PNP).

TRAPPIST-South is funded by the Belgian Fund for Scientific Research (Fond National de la Recherche Scientifique; FNRS) under the grant FRFC 2.5.594.09.F, with the participation of the Swiss National Science Foundation (SNF). M.G. and E.J. are F.R.S.-FNRS Research Directors.

This work is partly supported by JSPS KAKENHI Grant Numbers JP24H00017, JP24K00689, and JSPS Bilateral Program Number JPJSBP120249910. This paper is based on observations made with the MuSCAT2 instrument, developed by ABC, at Telescopio Carlos Sánchez operated on the island of Tenerife by the IAC in the Spanish Observatorio del Teide.

## Appendix A
## Final Model Corner Plots

Figure 13 provides the corner plot of posteriors for WASP-102 b. The complete set of corner plots for all sources is available as a figure set in the online Journal.

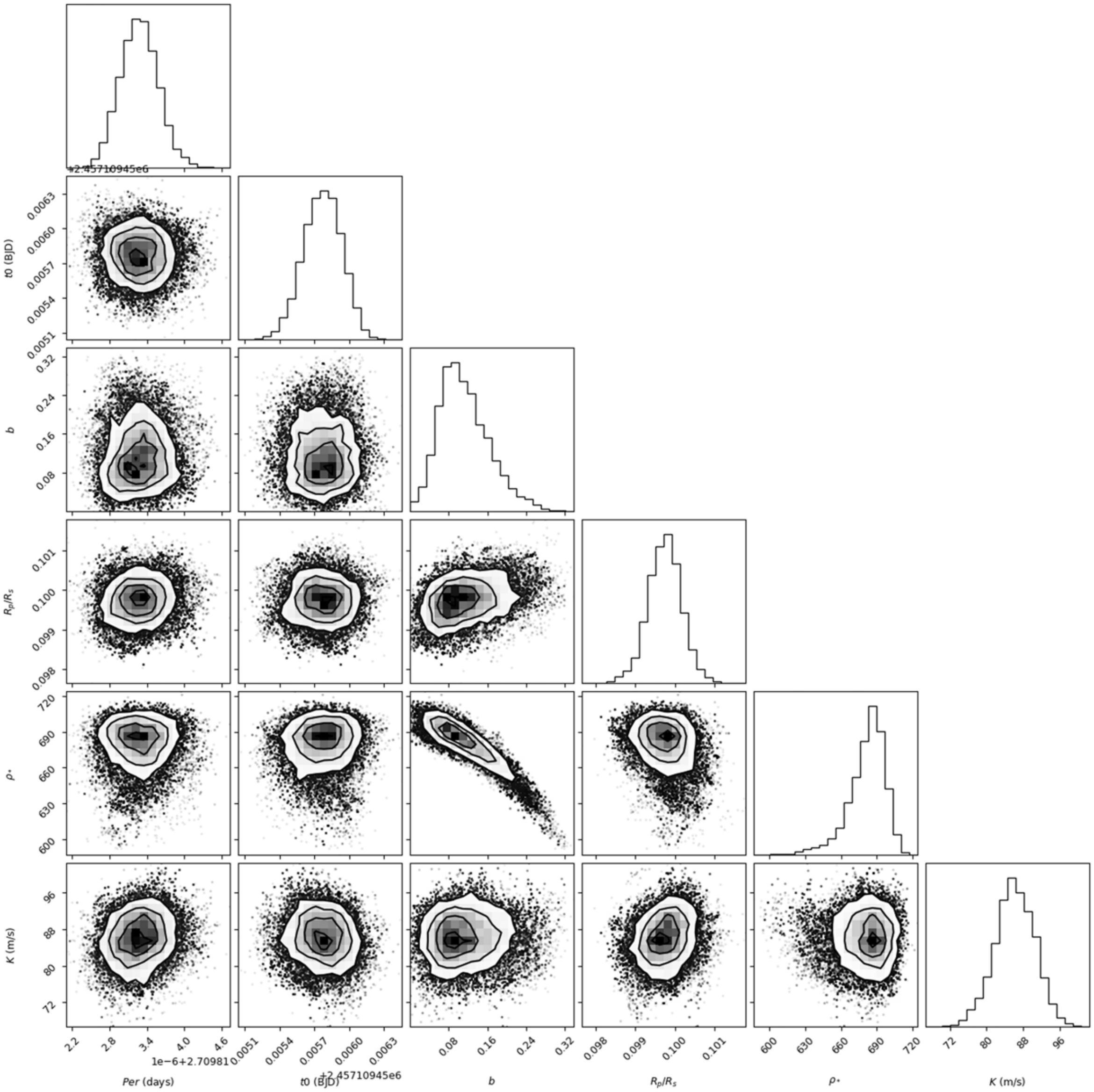

**Figure 13.** Corner plot showing posteriors for the fitted planet parameters for WASP-102 b. The complete set of corner plots (9 images) is available as a figure set in the online article.

(The complete figure set (9 images) is available in the online article.)

## Appendix B
## Full List of Model Parameter Priors and Posteriors

This appendix shows the model parameters along with the prior and posterior values used in the global juliet model. $\mathcal{N}$ priors indicate normal priors, $\mathcal{U}$ indicate uniform priors, and and ln$\mathcal{N}$ indicate log normal distributions. Table 7 provides the fit parameters for WASP-102 (TOI-6170). The complete set of fit parameters is available in the online Journal in a machine-readable format. See the juliet documentation[49] for further details on the parameters.

---

[49] https://juliet.readthedocs.io/en/latest/user/priorsnparameters.html

**Table 7**
Transit Fit Parameters for WASP-102 (TOI-6170)

| Parameter | Prior | Fit Value |
|---|---|---|
| P_p1 | $\mathcal{N}(2.7098094867,0.0002372)$ | $2.7098132718^{3.016e-07}_{3.04e-07}$ |
| t0_p1 | $\mathcal{N}(2457109.458301,0.01)$ | $2457109.4557701275^{0.0001614387}_{0.0001695896}$ |
| b_p1 | $\mathcal{U}(0.0,1.0)$ | $0.1053561292^{0.0586122843}_{0.0416958994}$ |
| p_p1 | $\mathcal{N}(0.09999466,0.1)$ | $0.0997457844^{0.0003999763}_{0.0004126752}$ |
| rho | $\mathcal{N}(585,100)$ | $684.03713543^{11.4262294054}_{16.4163205423}$ |
| q1_TESS_WASP | $\mathcal{N}(0.303,0.05)$ | $0.21933795^{0.027931697}_{0.0348288851}$ |
| q2_TESS_WASP | $\mathcal{N}(0.383,0.05)$ | $0.3462643271^{0.0348421143}_{0.0367554598}$ |
| q1_EULER1 | $\mathcal{N}(0.418,0.05)$ | $0.429942767^{0.029506276}_{0.027943585}$ |
| q2_EULER1 | $\mathcal{N}(0.397,0.05)$ | $0.3841748256^{0.0359090282}_{0.0392379723}$ |
| q1_EULER2 | $\mathcal{N}(0.310,0.05)$ | $0.3093626479^{0.0335669181}_{0.0381012247}$ |
| q2_EULER2 | $\mathcal{N}(0.385,0.05)$ | $0.3803861446^{0.0384892142}_{0.0355197112}$ |
| q1_TRAPPIST1_TRAPPIST2_TRAPPIST3 | $\mathcal{N}(0.30349081,0.05)$ | $0.3537181002^{0.0307973873}_{0.031618477}$ |
| q2_TRAPPIST1_TRAPPIST2_TRAPPIST3 | $\mathcal{N}(0.38273734,0.05)$ | $0.4151080521^{0.0348155047}_{0.0306933365}$ |
| mdilution_TESS | $\mathcal{N}(1.0,0.01)$ | $0.9869754783^{0.007289593}_{0.0084533815}$ |
| mflux_TESS | $\mathcal{N}(0.0,0.01)$ | $-0.0001342711^{6.345e-05}_{6.44869e-05}$ |
| sigma_w_TESS | $\ln\mathcal{N}(1e-06,1000000.0)$ | $0.0032181223^{0.985238121}_{0.0031955477}$ |
| mdilution_WASP | $\mathcal{N}(1.0,0.01)$ | $0.9973126254^{0.0086343868}_{0.0083784906}$ |
| mflux_WASP | $\mathcal{N}(0.0,0.01)$ | $-0.0005717013^{0.000109142}_{0.000103488}$ |
| sigma_w_WASP | $\ln\mathcal{N}(1e-06,1000000.0)$ | $3297.6306980352^{257.6755241177}_{232.7289360615}$ |
| mdilution_EULER1 | $\mathcal{N}(1.0,0.01)$ | $1.0074198988^{0.0073958711}_{0.0061536879}$ |
| mflux_EULER1 | $\mathcal{N}(0.0,0.01)$ | $0.0033593069^{0.0011068267}_{0.0010334332}$ |
| sigma_w_EULER1 | $\ln\mathcal{N}(1e-06,1000000.0)$ | $439.6844804777^{108.9069736517}_{109.7533915897}$ |
| theta0_EULER1 | $\mathcal{U}(-100,100)$ | $0.0019320809^{0.0006875206}_{0.0006326413}$ |
| mdilution_EULER2 | $\mathcal{N}(1.0,0.01)$ | $0.9919475645^{0.0068671264}_{0.0080144526}$ |
| mflux_EULER2 | $\mathcal{N}(0.0,0.01)$ | $-0.0019202767^{0.0010189849}_{0.0011670411}$ |
| sigma_w_EULER2 | $\ln\mathcal{N}(1e-06,1000000.0)$ | $993.9563169572^{92.5340345654}_{92.4165864685}$ |
| theta0_EULER2 | $\mathcal{U}(-100,100)$ | $-0.0009325131^{0.0006287706}_{0.0007489514}$ |
| mdilution_TRAPPIST1 | $\mathcal{N}(1.0,0.01)$ | $1.0223432356^{0.0090554794}_{0.0080193752}$ |
| mflux_TRAPPIST1 | $\mathcal{N}(0.0,0.01)$ | $-0.0023889443^{0.0004810746}_{0.0004375614}$ |
| sigma_w_TRAPPIST1 | $\ln\mathcal{N}(1e-06,1000000.0)$ | $1222.9486938427^{89.2332773471}_{87.1378057286}$ |
| theta0_TRAPPIST1 | $\mathcal{U}(-100,100)$ | $-0.0010845235^{0.0002741073}_{0.000255327}$ |
| mdilution_TRAPPIST2 | $\mathcal{N}(1.0,0.01)$ | $1.0030891272^{0.009156801}_{0.0076036294}$ |
| mflux_TRAPPIST2 | $\mathcal{N}(0.0,0.01)$ | $0.0031180731^{0.0008245315}_{0.0009136841}$ |
| sigma_w_TRAPPIST2 | $\ln\mathcal{N}(1e-06,1000000.0)$ | $3392.037458069^{115.011594554}_{109.4153474344}$ |
| theta0_TRAPPIST2 | $\mathcal{U}(-100,100)$ | $0.0021688568^{0.0004704801}_{0.0005199252}$ |
| mdilution_TRAPPIST3 | $\mathcal{N}(1.0,0.01)$ | $0.9883415703^{0.0080450539}_{0.009753062}$ |
| mflux_TRAPPIST3 | $\mathcal{N}(0.0,0.01)$ | $-0.0002547559^{0.0005762263}_{0.0005222762}$ |
| sigma_w_TRAPPIST3 | $\ln\mathcal{N}(1e-06,1000000.0)$ | $1181.1269937596^{124.79770027}_{132.2603944195}$ |
| theta0_TRAPPIST3 | $\mathcal{U}(-100,100)$ | $0.0008109566^{0.0003061372}_{0.0002816134}$ |
| GP_sigma_TESS | $\ln\mathcal{N}(1e-06,1000000.0)$ | $0.0004986827^{4.34615e-05}_{3.77943e-05}$ |
| GP_rho_TESS | $\ln\mathcal{N}(0.001,1.0)$ | $0.2231794777^{0.0492960748}_{0.0376425229}$ |
| K_p1 | $\mathcal{U}(0,200)$ | $86.1550827174^{4.3719118508}_{4.2811423179}$ |
| sigma_w_SOPHIE | $\ln\mathcal{N}(0.001,100.0)$ | $0.1051695987^{1.2480695501}_{0.0976563169}$ |
| mu_SOPHIE | $\mathcal{U}(-200,200)$ | $-1.3939161961^{3.8244593735}_{4.108173765}$ |
| sigma_w_CORALIE | $\ln\mathcal{N}(0.001,100.0)$ | $0.0941341935^{1.5615415191}_{0.0883157186}$ |
| mu_CORALIE | $\mathcal{U}(-200,200)$ | $-24.0994459181^{5.3171361087}_{5.4130000819}$ |

**Notes.** The complete set of fit parameters is available in the machine-readable format in the online Journal

(This table is available in its entirety in machine-readable form in the online article.)

## Appendix C
## High-resolution Imaging of Host Stars

Figure 14 shows high-resolution images used to identify nearby companion stars. The complete set of high-resolution images is available as a figure set in the online Journal.

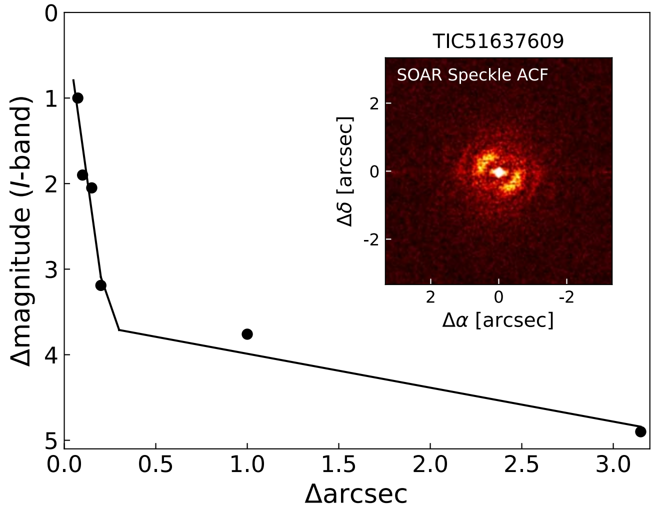

**Figure 14.** High-resolution images of WASP-102 taken by HRCam. The complete set of high-resolution images (9 images) is available as a figure set in the online article.

(The complete figure set (9 images) is available in the online article.)

## ORCID iDs

K.G. Stassun https://orcid.org/0000-0002-3481-9052
B. Hord https://orcid.org/0000-0001-5084-4269
K. Barkaoui https://orcid.org/0000-0003-1464-9276
A. Bieryla https://orcid.org/0000-0001-6637-5401
D. Ciardi https://orcid.org/0000-0002-5741-3047
K.A. Collins https://orcid.org/0000-0001-6588-9574
A. Collier Cameron https://orcid.org/0000-0002-8863-7828
J. Hartman https://orcid.org/0000-0001-8732-6166
C. Hellier https://orcid.org/0000-0002-3439-1439
S.B. Howell https://orcid.org/0000-0002-2532-2853
M. Lendl https://orcid.org/0000-0001-9699-1459
J. McCormac https://orcid.org/0000-0003-1631-4170
K.K. McLeod https://orcid.org/0000-0001-9504-1486
H. Parviainen https://orcid.org/0000-0001-5519-1391
D. Radford https://orcid.org/0000-0002-3940-2360
H. Relles https://orcid.org/0009-0009-5132-9520
S. Baliwal https://orcid.org/0000-0001-8998-3223
G. Bakos https://orcid.org/0000-0001-7204-6727
S. C. C. Barros https://orcid.org/0000-0003-2434-3625
F. Bouchy https://orcid.org/0000-0002-7613-393X
A. Burdanov https://orcid.org/0000-0001-9892-2406
C. Clark https://orcid.org/0000-0002-2361-5812
Laetitia Delrez https://orcid.org/0000-0001-6108-4808
M. Everett https://orcid.org/0000-0002-0885-7215
M. Gillon https://orcid.org/0000-0003-1462-7739
Akihiko Fukui https://orcid.org/0000-0002-4909-5763
C. Hedges https://orcid.org/0000-0002-3385-8391
E. Jehin https://orcid.org/0000-0001-8923-488X
J.M. Jenkins https://orcid.org/0000-0002-4715-9460
D. Laloum https://orcid.org/0000-0002-8515-955X
John Livingston https://orcid.org/0000-0002-4881-3620
P. Maxted https://orcid.org/0000-0003-3794-1317
I. Mireles https://orcid.org/0000-0002-4510-2268
Felipe Murgas https://orcid.org/0000-0001-9087-1245
N. Narita https://orcid.org/0000-0001-8511-2981
Enric Palle https://orcid.org/0000-0003-0987-1593
M. Rose https://orcid.org/0000-0003-4724-745X
S.G. Sousa https://orcid.org/0000-0001-9047-2965
A. Tuson https://orcid.org/0000-0002-2830-9064
J. Winn https://orcid.org/0000-0002-4265-047X

## References

Anderson, D. R., Collier Cameron, A., Delrez, L., et al. 2014, MNRAS, 445, 1114
Bakos, G., Noyes, R. W., Kovács, G., et al. 2004, PASP, 116, 266
Bakos, G. A., Torres, G., Pál, A., et al. 2010, ApJ, 710, 1724
Baliwal, S., Sharma, R., Chakraborty, A., et al. 2024, A&A, 691, A12
Barbary, K., Boone, K., McCully, C., et al. 2016, kbarbary/sep, v1.0.0, Zenodo, doi:10.5281/zenodo.159035
Bertin, E., & Arnouts, S. 1996, A&AS, 117, 393
Bouchy, F., Hébrard, G., Udry, S., et al. 2009, A&A, 505, 853
Brown, D. J. A., Anderson, D. R., Doyle, A. P., et al. 2014, arXiv:1412.7761
Brown, T. M., Baliber, N., Bianco, F. B., et al. 2013, PASP, 125, 1031
Buchhave, L. A., Bakos, G. A., Hartman, J. D., et al. 2010, ApJ, 720, 1118
Buchhave, L. A., Latham, D., Johansen, A., et al. 2012, Natur, 486, 375
Caldwell, D. A., Tenenbaum, P., Twicken, J. D., et al. 2020, RNAAS, 4, 201
Chakraborty, A., Bharadwaj, K. K., Siva Sehu Vara Prasad Neelam, J., et al. 2024, BSRSL, 93, 68
Chakraborty, A., Mahadevan, S., Roy, A., et al. 2014, PASP, 126, 133
Chakraborty, A., Roy, A., Sharma, R., et al. 2018, AJ, 156, 3
Chaturvedi, P., Chakraborty, A., Anandarao, B. G., Roy, A., & Mahadevan, S. 2016, MNRAS, 462, 554
Ciardi, D. R., Beichman, C. A., Horch, E. P., & Howell, S. B. 2015, ApJ, 805, 16
Collier Cameron, A., Guenther, E., Smalley, B., et al. 2010, MNRAS, 407, 507
Collins, K. A., Kielkopf, J. F., Stassun, K. G., & Hessman, F. V. 2017, AJ, 153, 77
Craig, M. W., Crawford, S. M., Deil, C., et al., 2015 ccdproc: CCD Data Reduction Software, Astrophysics Source Code Library, ascl:1510.007
Dawson, R. I., & Johnson, J. A. 2018, ARA&A, 56, 175
Dawson, R. I., Murray-Clay, R. A., & Johnson, J. A. 2015, ApJ, 798, 66
Dekany, R., Roberts, J., Burruss, R., et al. 2013, ApJ, 776, 130
Demory, B.-O., & Seager, S. 2011, ApJS, 197, 12
Espinoza, N., Kossakowski, D., & Brahm, R. 2019, MNRAS, 490, 2262
Faedi, F., Gómez Maqueo Chew, Y., Pollacco, D., et al. 2016, arXiv:1608.04225
Fortney, J. J., Dawson, R. I., & Komacek, T. D. 2021, JGRE, 126, e2020JE006629
Furész, G. 2008, PhD thesis, Univ. Szeged, Hungary
Furlan, E., Ciardi, D. R., Everett, M. E., et al. 2017, AJ, 153, 71
Gaia Collaboration, Brown, A. G. A., Vallenari, A., et al. 2021, A&A, 649, A1
Gillon, M., Jehin, E., Magain, P., et al. 2011, EPJ Web Conf., 11, 06002
Guerrero, N. M., Seager, S., Huang, C. X., et al. 2021, ApJS, 254, 39
Hayward, T. L., Brandl, B., Pirger, B., et al. 2001, PASP, 113, 105
Hebb, L., Collier-Cameron, A., Loeillet, B., et al. 2009, ApJ, 693, 1920
Heidari, N., Boisse, I., Hara, N. C., et al. 2024, A&A, 681, A55
Howell, S. B., Everett, M. E., Sherry, W., Horch, E., & Ciardi, D. R. 2011, AJ, 142, 19
Huang, C. X., Vanderburg, A., Pál, A., et al. 2020a, RNAAS, 4, 204
Huang, C. X., Vanderburg, A., Pál, A., et al. 2020b, RNAAS, 4, 206
Husser, T. O., Wende-von Berg, S., Dreizler, S., et al. 2013, A&A, 553, A6
Jeffreys, H. 1939, Theory of Probability (Oxford: Oxford Univ. Press),
Jehin, E., Gillon, M., Queloz, D., et al. 2011, Msngr, 145, 2
Jenkins, J. M., Twicken, J. D., McCauliff, S., et al. 2016, Proc. SPIE, 9913, 99133E
Karalis, A., Lee, E. J., & Thorngren, D. P. 2025, ApJ, 978, 46
Kempton, E. M. R., Bean, J. L., Louie, D. R., et al. 2018, PASP, 130, 114401
Kipping, D. M. 2013, MNRAS, 435, 2152
Kovács, G., Bakos, G., & Noyes, R. W. 2005, MNRAS, 356, 557
Kovács, G., Zucker, S., & Mazeh, T. 2002, A&A, 391, 369
Kunimoto, M., Daylan, T., Guerrero, N., et al. 2022, ApJS, 259, 33
Kurucz, R. L. 1992, in IAU Symp. 149, The Stellar Populations of Galaxies, ed. B. Barbuy & A. Renzini (Cambridge: Cambridge Univ. Press), 225
Kurucz, R. L. 1993, SYNTHE Spectrum Synthesis Programs and Line Data [CDROM] (Cambridge, MA: Smithsonian Astrophysical Observatory)
Lee, E. J., & Chiang, E. 2016, ApJ, 817, 90

Lendl, M., Anderson, D. R., Collier-Cameron, A., et al. 2012, A&A, 544, A72
Lester, K. V., Matson, R. A., Howell, S. B., et al. 2021, AJ, 162, 75
Libby-Roberts, J. E., Berta-Thompson, Z. K., Désert, J.-M., et al. 2020, AJ, 159, 57
Mamajek, E. E., & Hillenbrand, L. A. 2008, ApJ, 687, 1264
Matson, R. A., Howell, S. B., Horch, E. P., & Everett, M. E. 2018, AJ, 156, 31
McCormac, J., Pollacco, D., Skillen, I., et al. 2013, PASP, 125, 548
McCormac, J., Skillen, I., Pollacco, D., et al. 2014, MNRAS, 438, 3383
McCully, C., Volgenau, N. H., Harbeck, D.-R., et al. 2018, Proc. SPIE, 10707, 107070K
Mol Lous, M., & Miguel, Y. 2020, MNRAS, 495, 2994
Narita, N., Fukui, A., Kusakabe, N., et al. 2019, JATIS, 5, 015001
Owen, J. E., & Wu, Y. 2016, ApJ, 817, 107
Parviainen, H. 2015, MNRAS, 450, 3233
Parviainen, H., & Aigrain, S. 2015, MNRAS, 453, 3821
Parviainen, H., Tingley, B., Deeg, H. J., et al. 2019, A&A, 630, A89
Perruchot, S., Kohler, D., Bouchy, F., et al. 2008, Proc. SPIE, 7014, 70140J
Piskunov, N. E., & Valenti, J. A. 2002, A&A, 385, 1095
Pollacco, D. L., Skillen, I., Collier Cameron, A., et al. 2006, PASP, 118, 1407
Queloz, D., Henry, G. W., Sivan, J. P., et al. 2001, A&A, 379, 279
Queloz, D., Mayor, M., Weber, L., et al. 2000, A&A, 354, 99
Ricker, G. R., Winn, J. N., Vanderspek, R., et al. 2015, JATIS, 1, 014003
Schanche, N., Collier Cameron, A., Almenara, J. M., et al. 2019a, MNRAS, 488, 4905
Schanche, N., Collier Cameron, A., Hébrard, G., et al. 2019b, MNRAS, 483, 5534
Schlegel, D. J., Finkbeiner, D. P., & Davis, M. 1998, ApJ, 500, 525
Scott, N. J., Howell, S. B., Gnilka, C. L., et al. 2021, FrASS, 8, 138
Scott, N. J., Howell, S. B., Horch, E. P., & Everett, M. E. 2018, PASP, 130, 054502
Smith, J. C., Stumpe, M. C., Van Cleve, J. E., et al. 2012, PASP, 124, 1000
Sneden, C. A. 1973, PhD thesis, Univ. Texas, Austin
Sousa, S. G., Adibekyan, V., Delgado-Mena, E., et al. 2021, A&A, 656, A53
Sousa, S. G., Santos, N. C., Adibekyan, V., Delgado-Mena, E., & Israelian, G. 2015, A&A, 577, A67
Sousa, S. G., Santos, N. C., Mayor, M., et al. 2008, A&A, 487, 373
Spake, J. J., Oklopčić, A., & Hillenbrand, L. A. 2021, AJ, 162, 284
Speagle, J. S. 2020, MNRAS, 493, 3132
Stassun, K. G., Collins, K. A., & Gaudi, B. S. 2017, AJ, 153, 136
Stassun, K. G., Corsaro, E., Pepper, J. A., & Gaudi, B. S. 2018, AJ, 155, 22
Stassun, K. G., & Torres, G. 2016, AJ, 152, 180
Strakhov, I. A., Safonov, B. S., & Cheryasov, D. V. 2023, AstBu, 78, 234
Stumpe, M. C., Smith, J. C., Catanzarite, J. H., et al. 2014, PASP, 126, 100
Stumpe, M. C., Smith, J. C., Van Cleve, J. E., et al. 2012, PASP, 124, 985
Tamuz, O., Mazeh, T., & Zucker, S. 2005, MNRAS, 356, 1466
Tokovinin, A. 2018, PASP, 130, 035002
Torres, G., Andersen, J., & Giménez, A. 2010, A&ARv, 18, 67
Twicken, J. D., Catanzarite, J. H., Clarke, B. D., et al. 2018, PASP, 130, 064502
Tyler, D., Petigura, E. A., Oklopčić, A., & David, T. J. 2024, ApJ, 960, 123
Yee, S. W., Winn, J. N., Knutson, H. A., et al. 2020, ApJL, 888, L5
Ziegler, C., Tokovinin, A., Briceño, C., et al. 2020, AJ, 159, 19